

UnMarker: A Universal Attack on Defensive Watermarking

Andre Kassis and Urs Hengartner

{akassis,urs.hengartner}@uwaterloo.ca

University of Waterloo

Waterloo, Ontario, Canada

ABSTRACT

Reports regarding the misuse of *Generative AI (GenAI)* to create harmful deepfakes are emerging daily. Recently, defensive watermarking, which enables *GenAI* providers to hide fingerprints in their images to later use for deepfake detection, has been on the rise. Yet, its potential has not been fully explored. We present *UnMarker*—the first practical *universal* attack on defensive watermarking. Unlike existing attacks, *UnMarker* requires no detector feedback, no unrealistic knowledge of the scheme or similar models, and no advanced denoising pipelines that may not be available. Instead, being the product of an in-depth analysis of the watermarking paradigm revealing that robust schemes must construct their watermarks in the spectral amplitudes, *UnMarker* employs two novel adversarial optimizations to disrupt the spectra of watermarked images, erasing the watermarks. Evaluations against the *SOTA* prove its effectiveness, not only defeating traditional schemes while retaining superior quality compared to existing attacks but also breaking *semantic* watermarks that alter the image’s structure, reducing the best detection rate to 43% and rendering them useless. To our knowledge, *UnMarker* is the first practical attack on *semantic* watermarks, which have been deemed the future of robust watermarking. *UnMarker* casts doubts on the very penitential of this countermeasure and exposes its paradoxical nature as designing schemes for robustness inevitably compromises other robustness aspects.

CCS CONCEPTS

• Security and privacy → Authentication; Authorization; Social network security and privacy.

KEYWORDS

Deepfake Watermarking, Adversarial ML, Black-Box, Query-Free

1 INTRODUCTION

GenAI has amassed popularity due to its growing sophistication [14] and accessibility [2, 5, 6]. This technology has solved problems in various fields [16, 21, 41, 50, 57, 59]. Yet, it comes with the risk of malicious entities misusing it to generate harmful images (deepfakes) [19, 30], proven by the many reports of deepfakes used in political smear campaigns [7] and non-consensual pornography [27].

Defenses first emerged as passive detectors [13, 23, 33, 42, 70] that tell apart fake from real images, but these were proven ineffective, failing to generalize to unseen synthesis algorithms [15]. As training advanced generators is costly and prohibitive [36] in the absence of the extensive resources and high-quality data that only a few *GenAI* providers possess, adversaries typically resort to these providers’ APIs to generate harmful content. This recently led to the adoption of defensive watermarking as a countermeasure, which enables providers to embed hidden signatures in their images that can later

be identified using designated detectors. Defensive watermarking has gained traction in the research community [22, 46, 60, 63, 65–68, 72, 74] and the industry, as providers have already implemented and are testing such solutions (e.g., Google’s *SynthID* [25]) or pledged to do so soon [9] in commitments to the *White House* [28].

Defensive watermarking protects against limited adversaries, following the assumption that attackers lack the resources to train complex generators. Yet, existing schemes fail to demonstrate strong guarantees for this resistance beyond empirical robustness to naive manipulations. We devise *UnMarker*—the first *universal* (effective against **all** schemes), *black-box* (without access to the scheme’s parameters or similar systems), *data-free* (no additional data needed) and *query-free* (does not rely on detector feedback) attack.

Our motivating insight is that, for any scheme, there must be a *universal carrier* that embeds the watermark in all images. In layman’s terms, this *carrier* is the set of all image attributes the detector may examine when verifying the watermark. This set must exist and is also finite (shared among all images) since detectors are computationally limited. By analyzing the desired resistance to basic manipulations and the requirement that watermarks must naturally integrate with various contents, we deduce that this *carrier* can **only** be in spectral amplitudes. That is, a “conventionally” robust scheme *must* construct its watermarks by manipulating the frequencies at which the different pixels vary, forcing the *collective* distribution of pixel value shifts at different rates to follow a unique pattern. We can roughly even isolate the frequency range in which watermarks are encoded: the more robust *semantic* schemes [60, 63], which alter the structure, manipulate low frequencies while content-preserving *non-semantic* watermarks [22, 46, 66, 74] populate higher bands.

UnMarker thus adversarially disrupts these spectral amplitudes. To remove *non-semantic* watermarks, *UnMarker* directly modifies the image to optimize a designated loss, significantly affecting the rates at which *individual* pixels vary w.r.t. their neighbors, drastically affecting the distribution of high-frequency amplitudes. For *semantic* watermarks, we devise a novel class of optimizable filters and a procedure to learn their weights to *systemically* alter the consistency at different regions, causing discrepancies at lower frequencies. Unlike known filters that rely on geometric heuristics, limiting them to insignificant distortions, *UnMarker* is guided by a perceptual loss to maximize the disturbance in visually non-critical areas without compromising quality. As a result, the spectral *carrier* set is shifted away from the watermark’s distribution. By targeting the *carrier*, *UnMarker* abandons the dependence on a specific model, leaving it successful without knowledge of the scheme or detector feedback. Previous adversarial attacks [8, 32, 34, 45, 53, 62] all face this limitation, causing them to fail under realistic conditions.

We experiment with seven *SOTA* schemes from top venues. By combining the above techniques with *mild cropping* (10%), *UnMarker* breaks them all, despite its *black-box* and *query-free* nature.

We compare *UnMarker* with the recent *VAEAttack* [71] and *DiffusionAttack* [8, 53, 71], demonstrating far superior results, defeating *semantic* watermarks against which they fail and disputing misconceptions regarding these schemes’ robustness to limited adversaries [8, 53, 71]. Our results urge vendors to rethink their response to deepfakes. We make the following contributions:

- We thoroughly analyze defensive watermarking and reveal trade-offs that make it an invalid deepfake countermeasure.
- We present *UnMarker*, the first *universally-effective data-free, black-box, and query-free* attack against defensive watermarking¹. *UnMarker*’s success is due to its novel spectral optimizations.
- We demonstrate *UnMarker*’s efficacy against seven *SOTA* schemes under restrictive settings, rendering them of no practical use.
- We compare *UnMarker* to the most powerful *black-box* and *query-free* attacks, showing superior performance and image quality.
- Using a novel class of optimizable filters to incur structural disturbances, *UnMarker* is the first practical attack to defeat *semantic* watermarks, whose previous unparalleled robustness has marked them as the ultimate candidates for future trustworthy deepfake detection, casting doubts on the feasibility of this task.

2 BACKGROUND & RELATED WORK

Here, we provide related work on deepfake detection and defensive watermarking. We survey image synthesis techniques in A.1.

2.1 Deepfake Detection

Passive Detectors. They distinguish between real and fake images [13, 23, 33, 42, 70] based on semantic incoherences [31, 48] and low-level artifacts [13, 23, 33, 47, 51, 64] in deepfakes due to computational limitations. As proven in the image [12, 20] and audio domains [39], advanced generators can produce high-quality outputs without such telltales, and post-processing manipulations can fool these detectors that also fail to generalize to new systems [15].

Defensive Watermarking. It assumes limited attackers compared to *GenAI* providers, lacking the resources or data to train high-quality generators. A watermarking scheme consists of *watermark* (w), *encoder* (\mathcal{E}) and *detector* (\mathcal{D}). In a *general-purpose* scheme [60, 67, 74], \mathcal{E} accepts an arbitrary image x and outputs a similar watermarked $x_w = \mathcal{E}(x, w)$. Given image x' , \mathcal{D} extracts a sequence $w' = \mathcal{D}(x')$ that will be *almost* identical to w *iff* x' was previously watermarked. *Generator-specific* approaches “watermark” generative models: The encoder \mathcal{E} can be the generator \mathcal{G} itself that is trained to only produce watermarked images [65, 66] or an algorithm that modifies \mathcal{G} ’s weights [22, 46] or latent codes [63] s.t. every image it produces embeds the watermark. Heuristics-based watermarks [10, 49, 56, 63] *directly* manipulate spectral representations [10, 49, 56], forming a signature in select frequencies. These are removable via post-processing such as *JPEG* [22, 34, 74]. We focus on learning-based methods [22, 46, 60, 63, 65–68, 73, 74], where \mathcal{E} and \mathcal{D} are *DNNs* as they are robust to post-processing.

Semantic vs. Non-Semantic: *Non-semantic* schemes take an image and produce a visually identical watermarked version. Aside from

StegaStamp [60], all *general-purpose* schemes [67, 68, 74] are *non-semantic*. *Generator-specific* schemes [22, 46, 65, 66], with the exception of *TRW* [63], are also *non-semantic*, as their training restricts them to output images identical to non-watermarked references.

Semantic watermarks can influence the content. This term was popularized by Wen et al. with their introduction of *TRW* [63] that alters the latent codes used by conditional text-to-image *Latent Diffusion Models (LDMs)* [52]. When providing a “random” code with an auxiliary phrase that controls the output, the *LDM* uses this code as a seed to generate an image matching the text (e.g. the phrase “a dog on a bike” leads the *LDM* to output an image of a dog riding a bike but the dog and bike will differ based on the seed). *TRW* injects a universal pattern in the Fourier transforms of all latent codes before generation. As a result, watermarked images will be different from non-watermarked ones but still satisfy the text. This leaves watermarks invisible despite being highly robust.

StegaStamp [60] precedes *TRW* and operates similar to its *general-purpose* counterparts. Yet, it is less stealthy, causing structural changes (see Fig 2). Still, its strategically distributed distortion ensures minimal visibility. In defensive watermarking, users cannot observe non-watermarked images, further hiding these nuances and making *StegaStamp* highly applicable. While *semantic watermarks* primarily refer to *TRW*, previous work recognizes the similarities in both schemes, distinguishing them as more robust [8, 53, 71]. Thus, we refer to *TRW* and *StegaStamp* as *semantic*.

2.2 Attacks Against Defensive Watermarking

Regeneration Attacks. Initially proposed by Zhao et al. [71], they rely on *Diffusion Models (DMs)* [58] (see §A.1) or *Variational Autoencoders* [40] to introduce noise and then reconstruct the images, restoring their quality after the watermark has been eliminated. Saberi et al. [53] explore similar attacks, and *WAVES* [8] repeatedly propagates images through the regeneration pipeline to maximize the disruption at the risk of decreasing the sample’s quality. All three works verify the vulnerability of *non-semantic* watermarks against which regeneration attacks offer theoretical guarantees. Yet, *semantic* schemes remain robust. While *WAVES* shows that *TRW* experiences some degradation, it only occurs at a considerable distortion, at which point the attack loses its validity (see §3).

Regeneration methods remain the only practical (*black-box* and *query-free*) attacks, but they fail against *semantic* watermarks. Their success, even against *non-semantic* schemes, also depends on the denoising pipelines’ fidelity (due to computational power and training data), often severely impacting quality (see §6.2.3). *UnMarker* is the first to defeat all watermarks while also abandoning the dependence on regeneration models, always ensuring quality.

Adversarial Attacks. Practical attacks must assume no access to the schemes’ internals (see §3). This makes traditional adversarial attacks that target the decision boundaries of a specific model ineffective. Thus, existing works make relaxing assumptions, failing to retain success under realistic conditions.

WEVADE [34] optimizes watermarked images by querying the detector and updating them accordingly until the watermark is no longer detected. However, detector feedback is not necessarily available (see §3), making it ineffective. Lukas et al. [45] propose

¹Our code will be made publicly available upon publication

powerful query-free adversarial attacks, but they assume unrealistic access to a generator with similar architecture and data (see §3).

Saberi et al. [53] propose a surrogate-based attack. The scheme is defeated by mounting an adversarial attack against the surrogate, which transfers to the target. Training the substitute requires non-watermarked samples from the provider’s distribution, violating the principles of defensive watermarking [8, 32] (see §3) as providers only release *watermarked* images and possess exclusive datasets. Still, the attack fails against the *semantic StegaStamp* without considerably affecting quality. *RD-IWAN* [62] shares similar pitfalls, requiring access to non-watermarked provider images.

WAVES [8] evaluates surrogate attacks specifically on *semantic* schemes: *StegaStamp* remains robust, while *TRW* is only affected under unrealistic access to its autoencoder or images generated by it with *different* watermarks, which is impractical as a provider only publishes images with its *single* identifying watermark. They also show how Saberi et al.’s [53] surrogate attack fails even against *non-semantic* schemes absent any non-watermarked provider images.

Hu et al.’s [32] ensemble surrogate attack requires no non-watermarked provider images. Yet, evaluations are restricted to surrogates and targets of the same scheme (training methods and objectives), leading to sufficient commonalities for transferability and violating the *black-box* setting. It also requires extensive resources (training 40-100 surrogates), data, and large perturbations, making it impractical. The paper does not consider *semantic* watermarks.

UnMarker waives all impractical assumptions, requires no data or prohibitive computational power (see §7), and preserves quality.

3 THREAT MODEL

Providers’ Goals. Providers wish to ensure their services are not used to spread disinformation. Thus, they watermark **all** released images. If suspicious images surface, providers invoke their detectors to test if they contain the watermark, proving them fake.

Providers’ Capabilities. Providers have sufficient resources and data to train *SOTA* generators. As is common practice [2, 6], their *APIs* allow restricted access, accepting queries (e.g., text) and returning watermarked images without revealing intermediate results.

Attacker’s Goals. Attackers attempt to generate real-looking harmful images by invoking the providers’ *APIs* and then using methods to 1) remove watermarks while 2) retaining quality.

Attacker’s Capabilities: Resources. Following the defensive watermarking assumptions (see §2), attackers lack high-quality data or extensive resources. Thus, training advanced models or surrogates for the providers’ generators [45] or detectors [53] is not possible. As some services [1] allow renting advanced hardware, they may access powerful machines. Yet, this can only be short-term due to high costs, not for training large models over numerous *GPU* hours. **Black-Box.** As many providers keep their algorithms and datasets secret (closed-source) [54], attackers have no whitebox access to (similar) models, data, or any information about the system.

Query-Free. It is unclear how defensive watermarking will be used as commercial systems are still in development or testing [25]. Yet, recent announcements [18] suggest detectors may not be exposed publicly but only accessible to providers and chosen entities to identify and purge fake content, forcing attacks to be developed without detector feedback and disqualifying query-based methods [34].

4 DESIGN PHILOSOPHY

Since the detector \mathcal{D} must be able to verify the watermark in **any** image, it should know where to find this watermark, meaning there must be a set of attributes, namely the *universal carrier*, that can be measured in all images to make this decision. Our analysis will reveal that identifying this set is possible since the requirements from a robust scheme eliminate all options except ***the spectral amplitudes***. Thus, any robust scheme will inject its watermarks in the collective magnitudes of the different frequency bands. We will also show how identifying this *carrier* enables attackers to mount destructive attacks that remove the watermark with minimal visual impact and no information regarding the system (see §5).

4.1 Uncovering The Universal Carrier

A detector \mathcal{D} is a computationally limited algorithm that can only monitor a finite set of attributes $P = \{p_b \mid b \in [B]\}$ (for some B) in all images. Deciding if the image is watermarked is based on whether (a subset of) P ’s attributes follow a *watermark property distribution* P_w that \mathcal{D} associates with the watermark. Thus, while P is a set of attributes, P_w is a distribution over P ’s values that identifies the watermark. Practically, there may be several patterns P_w pertaining to different subsets of P . We term P the *universal carrier* since it contains all the properties watermarks can influence.

Although P_w should allow watermarking images with different contents, its variance must still be sufficiently low to prevent detecting w in non-watermarked images, restricting it to a reasonably narrow vicinity. Thus, relatively small deviations in P ’s values will cause any watermarked image to violate this distribution P_w , removing the watermark without compromising quality. This attack requires no knowledge of the specific P_w , making it executable without feedback from \mathcal{D} as it is merely destructive to the channel that carries the watermark. Attackers must identify the *carrier* P and then devise a method to disrupt it in a quality-preserving manner, which depends on the content. To identify the *carrier* P , we first analyze the *trivial*, widely-accepted requirements [22, 46, 60, 63, 65, 66, 74] from a robust scheme:

Robust Watermarking Requirements. Universal Applicability:

The scheme must be able to watermark images of various concepts and scenes, and the watermark must always be detectable.

Universal Stealthiness. The process cannot introduce unnatural artifacts that degrade image quality. We do not require the watermark not to leave visible traces since *semantic* watermarks violate this concept by definition, allowing them to influence the structure. Yet, as users can only observe the final, watermarked images, image quality becomes the only metric for quantifying *stealthiness*.

Robustness to Manipulations. The watermark should resist known manipulations (e.g, *cropping*, *blurring*, *compression*).

4.1.1 Candidates. An image is characterized by its 1) *spatial structure*—the specific pixel values, and 2) *frequency distribution* or the rates at which values alternate between neighboring pixels. Thus, the *carrier* must reside in these channels.

Spatial Structure: Watermarks cannot be embedded in the pixel values as they make for an *unreliable carrier* that experiences sporadic variations (in the absence of a watermark) between images based on their contents (different images assign extremely different values to

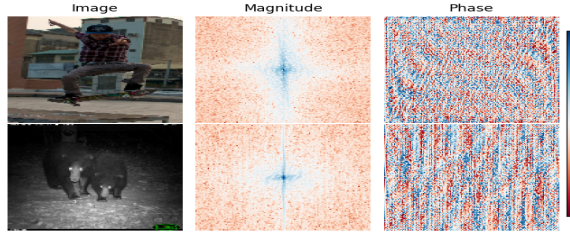


Figure 1: Spectral analysis of two images. Both depict worldly objects of high consistency. Thus, the *collective* spectral magnitudes are distributed similarly as the low frequencies (center) corresponding to gradual variations are always far more dominant. Phases determine the spatial arrangement of the pixel value shifts that constitute these magnitudes to shape the content, making them extremely different.

their pixels). However, the scheme must always bring the *carrier's* values to the same distribution P_w for any watermarked image. When these values naturally (i.e., without the watermark) exhibit a high degree of content dependency, this is impossible without restricting the scheme to processing a small set of similar contents or leaving unnatural cues in many outputs corresponding to contents that would otherwise require these values in images portraying them to lie far away from the desired P_w . As this distance increases, the magnitudes of the changes needed to bring them to P_w grow, failing to integrate naturally with the content. Restrictions violate *applicability*, while unnatural artifacts are not *stealthy*.

The scheme may strategically place the pixels encoding the watermark to accommodate large modifications with minimal visibility. Two possibilities exist: either they are far apart to remain unnoticeable despite significantly differing from their environments or located in regions the content is unlikely to occupy (i.e., the background). Both are volatile and cannot withstand manipulations (e.g., *cropping* or *noise*), violating the *robustness* requirement (see §6.2.1). Frequency Distribution: There are two options for influencing frequencies to inject watermarks: Locally or globally. Local modifications affect the rates at which pixels vary in select spatial regions. These share the above pitfalls, leaving only global changes to the spectrum. The spectrum associates frequencies with two properties: *magnitude* and *phase*. A frequency's magnitude represents the prevalence of shifts that occur at this rate across the image. Mathematically, any image is a superposition of periodic signals with varying frequencies occurring at different phases that determine their orientations and form the image's structure based on how they intersect. Phases vary drastically from image to image as the primary factor affecting the structure (see Fig. 1). Thus, they make for an *unreliable carrier* as well due to this sensitivity to the content.

Amplitudes are collective measurements with little dependency on specific pixels, making them resistant to reasonable manipulations that would preserve the majority of energy (amplitudes) distribution. They are also distributed similarly for any realistic content: lower frequencies contain the majority of energy as they correspond to gradual pixel changes that capture the inherent consistency (continuity) of the worldly objects images depict. Higher



Figure 2: Images watermarked by *StableSignature*— *non-semantic* (top), and *StegaStamp*— *semantic* (bottom). The rightmost figures display the differences between the original and watermarked images that correspond to the changes encoding the watermarks. *StableSignature's* modifications are restricted to existing (high-frequency) edges such as wrinkles, hair, mustache, and intersections of multiple components. *StegaStamp's* watermark is distributed across the image. The magnified area shows how it manipulates the consistency (texture), injecting gradual (low-frequency) changes that manifest as wrinkles at this location.

frequencies or rapid transitions occur at edges (intersections of multiple objects), making them far less prevalent (see Fig. 1). Thus, while amplitudes vary between images, they always follow a similar distribution, decaying as the frequencies grow. This stability that other alternatives lack allows injecting watermarks via changes of similar magnitudes for any content, enabling them to be minimized to an extent where they can always be integrated naturally.

4.1.2 Spectral Watermarks. The above entails that robust watermarks reside in the global spectral amplitudes. We now analyze how the different schemes achieve this while ensuring *stealthiness*: Non-Semantic: As they cannot change the content, these are typically injected in high frequencies since sufficiently manipulating lower bands s.t. the watermark is detected requires substantial changes due to the vast energy concentration in this range. To alter the collective distribution of high frequencies, polarization at *existing* edges can be controlled by adjusting the intensities of the various intersecting components to amplify or attenuate the transitions to their environments. This significantly impacts higher frequency amplitudes via small (invisible) modifications only due to the naturally low energy distribution in this range and by exploiting the characteristics of these regions (edges) that already exhibit high-frequency shifts to mask the watermark's footprint. Fig. 2 (top) depicts this behavior for the *non-semantic StableSignature* [22]. We verified that other *non-semantic* schemes operate similarly.

Semantic: Since they can influence the content, they will populate the consistency-defining low frequencies, making them more robust. As spectral amplitudes represent the *collective* contribution to pixel variations occurring at the relevant rates from all spatial locations, these schemes construct their outputs s.t. the needed changes are spread among different regions, reducing visual cues. Unlike *non-semantic* watermarks, they are not restricted to edges, affecting various objects' structures and textures. Since the changes

required to alter low-frequency magnitudes are large, their influence may be visible. Fig. 2 (bottom) portrays this for *StegaStamp* [60]. *TRW*'s [63] images may display different content from the original (non-watermarked), making illustrations uninformative (see §2.1). Yet, our results in §6.2.2 prove its watermarks are in low frequencies.

5 UNMARKER

Here, we present our universal attack. It follows from §4.1.1 that the *carrier* must be a set $F_c = \{|F_b| : b \in [B]\}$ of spectral amplitudes and the *watermark property distribution*, denoted as F_w , is over these amplitudes. Let ℓ_d be a perceptual distance metric s.t. if $\ell_d(x, y) \leq t_{\ell_d}$ for some threshold t_{ℓ_d} , then x and y are visually similar. We can now formalize watermark removal:

Watermark Removal. (WR): Given watermarking algorithm \mathcal{A} whose carrier frequency set is $F_c = \{|F_b| : b \in [B]\}$ with watermark property distribution F_w , the watermark w is removable from x_w if there is an image x_{nw} s.t. $\ell_d(x_w, x_{nw}) \leq t_{\ell_d} \wedge F_c(x_{nw}) \not\sim F_w$.

Removing the watermark from x_w amounts to finding a visually similar x_{nw} for which F_c 's attributes deviate from the expected distribution F_w . Due to our black-box framework, the specific F_c is unknown. Instead, we seek x_{nw} that retains visual similarity but maximizes some collective spectral difference ℓ_F from x_w :

$$x_{nw} = \underset{x'}{\operatorname{argmax}} [\ell_F(x_w, x')] \quad \text{s.t. } \ell_d(x_w, x') \leq t_{\ell_d} \quad (1)$$

Maximizing the difference across all frequencies should lead to significant discrepancies in the values of F_c , forcing them to deviate from F_w . As *semantic* and *non-semantic* watermarks target different parts of the spectrum, we must craft a suitable attack strategy for each, identifying a proper loss function and optimization procedure.

5.1 Attacking Non-Semantic Watermarks

We now instantiate eq. (1) to defeat *non-semantic* watermarks, while §5.2 presents a method against *semantic* schemes. Following §4.1.1, *non-semantic* watermarks are in higher frequencies. Thus, we must disrupt this range without leaving visible cues. We present our high-frequency loss DFL and the visual loss ℓ_d , explaining how each step updates the input to arrive at a watermark-free output.

Spectral Loss ℓ_F . We propose the *Direct Fourier Loss* (DFL):

$$\forall x, y : DFL(x, y) = \|FT(x) - FT(y)\|_1 \quad (2)$$

where FT is the (2D) Fourier transform. DFL calculates the band-wise spectral differences between x and y , outputting the sum of their magnitudes. Optimizing DFL maximizes the amplitudes of the differences in the collective spectral representations between the sample being optimized and the watermarked image x_w , which leads to an output whose spectral magnitudes differ from x_w 's. Since the watermark is encoded in these amplitudes, it will be significantly disrupted, causing the detector to fail to recognize it. Yet, this is only guaranteed if the perturbation budget that controls the quality and similarity to the watermarked image is permissive enough for such significant distortions to occur. Luckily, this is true when disturbing high frequencies since the energy concentration in these bands, and accordingly, the watermark's footprint (as it

should be invisible) is naturally small. Thus, watermarks become volatile, as they can be interfered with via minute perturbations.

Perceptual Loss. *Learned Perceptual Losses (LPIPS)*: They model human vision [69]. After experimenting with several candidates, we found *DeepVGGLoss-LPIPS* [17] (*DVL*) for large images ($\geq 256 \times 256$) and *LPIPS-Alex* [69] (*Alex*) otherwise optimal regardless of the scheme. High-frequency modifications may cause sporadic peaks to appear. *Alex* fails to fathom the fragility of the larger images' higher resolution, often overlooking such singleton points despite being visible, while *DVL* better captures this phenomenon. As these images are larger, numerous invisible violations throughout them sufficiently affect the spectrum. For smaller images, this restrictive loss prioritizes less destructive disruptions despite more powerful alternatives being applicable because of the reduced resolution. Due to the low dimensionality, such perturbations will not suffice, and increasing the budget results in visible cues as *DVL* cannot distinguish between these nuances at this resolution. This problem is absent in low-frequency optimizations that are of a different nature (see §5.2), where *DVL* can be used with all sizes.

Norm Constraint: To further ensure no such peaks appear (especially for low resolutions), we also use the $\|\cdot\|_2$ norm to place a geometric bound on the distance from the watermarked image, allowing us to slightly increase the budget used for *LPIPS*. Whenever *LPIPS* risks introducing such peaks, $\|\cdot\|_2$ grows, forcing the procedure to explore different directions. Yet, $\|\cdot\|_2$ alone is insufficient since geometric constraints cannot capture visual similarity and will either lead to sub-optimal solutions if used with extremely small thresholds or impact quality otherwise. This is especially true since we operate in a *black-box* framework without model feedback, which raises the bar and requires larger perturbations, entailing that the perceptual loss should be accurate to preserve quality.

Final High-Frequency Destruction Procedure. (for *non-semantic* watermarks) Using the above components, we implement eq. (1). We only need to identify the rules for updating the sample to define our search space. Since we seek high-frequency disruptions that affect the rates at which *individual* pixels vary w.r.t. their neighbors (as opposed to collective low-frequency changes), we should modify each pixel directly at each step. Thus, our algorithm accepts watermarked image x_w , *LPIPS* loss ℓ_p , *LPIPS* threshold t_{ℓ_p} , and $\|\cdot\|_2$ threshold $t_{\|\cdot\|_2}$, and finds modifier δ that maximizes DFL as follows:

$$x_{nw} = x_w + \underset{\delta}{\operatorname{argmin}} \left[\begin{array}{c} c_{\ell_p} \cdot \operatorname{ReLU}_{\ell_p}(x_w + \delta, x_w) + c_{\|\cdot\|_2} \cdot \operatorname{ReLU}_{\|\cdot\|_2}(x_w + \delta, x_w) \\ - DFL(x_w + \delta, x_w) \end{array} \right] \quad (3)$$

For brevity, $\operatorname{ReLU}_{\ell}(x, y)$ denotes $\max\{\ell(x, y) - t_{\ell}, 0\}$ for any loss ℓ . Effectively, we instantiate ℓ_d from eq. (1) with two components: *LPIPS* loss ℓ_p and norm $\|\cdot\|_2$, each having its own threshold, while DFL is used as the spectral loss. δ is a vector that captures the changes introduced into x_w to generate the non-watermarked $x_{nw} = x_w + \delta$. We minimize $-DFL$, maximizing DFL . The constants c_{ℓ_p} and $c_{\|\cdot\|_2}$ balance the spectral and perceptual losses. For each of the perceptual loss (ℓ_d) components ℓ_p and $\|\cdot\|_2$, we enforce that they remain under respective thresholds t_{ℓ_p} and $t_{\|\cdot\|_2}$ through the term $\max\{\ell_d(x_w + \delta, x_w) - t_d, 0\}$: When ℓ_d exceeds t_{ℓ_d} , it evaluates to $\ell_d(x_w + \delta, x_w) - t_d$, causing ℓ_d 's gradients to participate in the back-propagation, leading to the sample in the next iteration being closer to x_w . Otherwise, it returns 0, discarding ℓ_d 's gradients

and maximizing DFL unconditionally. $c_{\|\cdot\|_2}$ is a fixed large coefficient that prevents the peaks described above. Meanwhile, c_{ℓ_p} is determined via a binary search: We start with a large c_{ℓ_p} , assigning a larger weight to ℓ_p 's gradients and run the optimization for a number of steps. If a solution is found, c_{ℓ_p} is decreased, making DFL more dominant and permitting the algorithm to increase the spectral distance at the expense of larger perceptual deviations. Otherwise, c_{ℓ_p} is amplified. Further details are in A.3.

5.2 Attacking Semantic Watermarks

Semantic watermarks reside in low frequencies, making them difficult to address. In addition to their large magnitudes (see §4.1.2), low frequencies correspond to many neighboring pixels varying gradually, indicating these watermarks are rooted in the image's objects' consistencies. Thus, removing them requires altering pixels *systemically* via structural changes to the different regions. Direct optimizations similar to §5.1 fail since they operate on the image and, at each step, individual pixels are updated in different directions. This targets higher frequencies, introducing significant changes yet *only* to a few pixels, failing to progress further due to the perceptual similarity constraint and incurring minimal changes at low frequencies. We could limit the procedure to optimize DFL over low-frequencies only. Yet, as significant changes are required in this range, without a methodical scheme, we will converge to a sub-optimal solution wherein a certain region receives substantial modifications, leading the perceptual loss to prevent further updates. This is because the process fails to account for inter-pixel links, and DFL does not spread the changes throughout the image.

We develop a visually-aware attack inspired by image filtering. While filters apply systemic spectral disruptions, they fail to remove watermarks due to their content-agnostic nature, limiting the distortions they may introduce without leaving crucial visual cues. Our adversarial alternative retains quality by learning the filters' weights to solve an optimization problem that maximizes low-frequency disruptions, resorting to a perceptual loss to preserve critical information. First, we motivate our design through guiding principles. We then provide technical details and present our optimizable filters. Finally, we introduce our system's components.

5.2.1 Motivation. Basic Filtering: An image is convolved with a filter ($M \times N$ *spectral kernel*), moved s.t. its center is aligned with a single pixel (i, j) at each step. The output at (i, j) is calculated by multiplying the kernel by the pixel's vicinity and summing over the product— see Fig. 3(a). The kernel's values are non-negative and sum to 1, making this output an averaged sum of the pixel and its neighbors. This performs noise reduction, decaying unwanted peaks. The kernel's elements grow toward the center, assigning a larger weight to the original pixel to preserve the content.

Convolution in the spatial domain translates to multiplication in the frequency space: Given the spectral representations of the image and filter, it produces an image with a spectrum equivalent to their product. Thus, filters are good candidates for spectral manipulations. Yet, the outputs at any pixel are calculated using the same kernel. Hence, their potential to remove watermarks is limited [46, 71] due to their content-agnostic nature, making them only applicable with mild parameters as stronger blurring impacts quality.

Guided Filtering: These advanced filters tackle the information loss under stronger distortions, allowing more effective noise reduction while preserving crucial data. They are edge-preserving, minimizing the distortion at these critical boundary points between different objects. Instead of using a uniform kernel, the process involves an additional per-pixel *color kernel* that weakens the filter at edge points based on geometric principles: If some values in the pixel's vicinity drastically differ from it, then it lies on an edge, as these neighbors belong to other components and the *spectral kernel*'s strength at this point must be diminished to preserve defining information. The *color kernel* computes a modulation factor for every neighbor in the filter's vicinity around (i, j) based on its value's difference from (i, j) 's. The *effective kernel* for calculating (i, j) 's output is the Hadamard product of the two kernels— see Fig. 3(b). Guided filters fail to remove watermarks despite allowing for stronger blurring (see §6.2.1) since they merely follow geometric heuristics that fail to fully capture human vision or target specific image characteristics, limiting the allowed distortion. In practice, less *visually-critical* areas can be changed drastically, regardless.

Adversarial Filtering (Our Attack): Based on the above, structure-aware filters can better maximize the spectral distortion with minimal impact on crucial regions. Similar to guided filters, we design a process for learning a set of per-pixel kernels. Yet, instead of relying on geometric heuristics, our method learns the kernels' parameters s.t. they retain *perceptual similarity* to the original image from a human's perspective, allowing for stronger filtering.

5.2.2 Formalizing Filters. Given image $I \in \mathbb{R}^{Q \times R}$, $PE_{M \times N}^{i, j} : \mathbb{R}^{Q \times R} \rightarrow \mathbb{R}^{M \times N}$ denotes the *local patch extractor* that outputs the $M \times N$ vicinity around its $(i, j)^{th}$ pixel s.t. this pixel is at the center of this patch (i.e., $PE_{M \times N}^{i, j}(I)(\lfloor \frac{M}{2} \rfloor, \lfloor \frac{N}{2} \rfloor) = I(i, j)$)— see Fig. 3(a). The *global patch extractor* $PE_{M \times N} : \mathbb{R}^{Q \times R} \rightarrow \mathbb{R}^{Q \times R \times M \times N}$ outputs a matrix storing $PE_{M \times N}^{i, j}$ for every (i, j) . That is, $PE_{M \times N}(I)$'s $(i, j)^{th}$ cell contains the $M \times N$ patch around the $(i, j)^{th}$ pixel. We now formalize different filters to present our solution.

Basic Filtering: Basic filters simply apply the known convolution with a fixed *spectral kernel* $\mathcal{K} \in \mathbb{R}^{M \times N}$. Denoting element-wise multiplication as \odot , these filters can be written as $\mathcal{F}_{\mathcal{K}} : \mathbb{R}^{Q \times R} \rightarrow \mathbb{R}^{Q \times R}$ s.t. $\mathcal{F}_{\mathcal{K}}(I)(i, j) = \sum_{m, n} PE_{M \times N}^{i, j}(I) \odot \mathcal{K}$ (see Fig. 3(a)).

Guided Filtering: These employ additional per-pixel *color kernels* to modulate distortions at critical points (Fig. 3(b)). Given kernel size $M \times N$, the *color kernel* for each (i, j) is the matrix whose (m, n)

cell is $C_{i, j}^{I, \sigma_c}(m, n) = e^{-\frac{\|I(i+m-\lfloor \frac{M}{2} \rfloor, j+n-\lfloor \frac{N}{2} \rfloor) - I(i, j)\|_1}{2\sigma_c^2}}$. σ_c is a permissiveness controlling the modulation intensity. The $\|\cdot\|_1$ norm accounts for each pixel potentially having multiple color channels. For instance, *RGB* images associate each pixel with three values. The *effective kernel* for computing the output at (i, j) is then $\mathcal{V}_{i, j}^{I, \mathcal{K}, \sigma_c} = \frac{C_{i, j}^{I, \sigma_c} \odot \mathcal{K}}{\sum_{m, n} C_{i, j}^{I, \sigma_c} \odot \mathcal{K}}$. At the center, $C_{i, j}^{I, \sigma_c}(\lfloor \frac{M}{2} \rfloor, \lfloor \frac{N}{2} \rfloor) = 1$, indicating the contribution of the original $I(i, j)$ is not decayed. For neighbors, large distances decrease their coefficients and limit their contributions. By defining $\mathcal{V}^{I, \mathcal{K}, \sigma_c}$ as the matrix whose $(i, j)^{th}$ cell contains $\mathcal{V}_{i, j}^{I, \mathcal{K}, \sigma_c}$, the guided filter is $GF_{\mathcal{K}, \sigma_c}(I) = \sum_{m, n} PE_{M \times N}(I) \odot \mathcal{V}^{I, \mathcal{K}, \sigma_c}$.

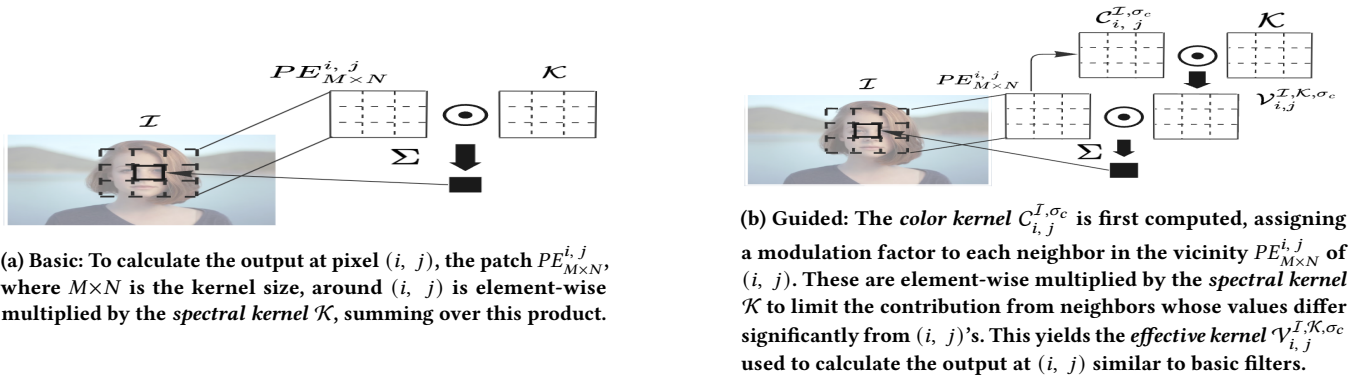


Figure 3: Operation of known filters.

Optimizable Filters (Ours): The drawback of guided filtering is that it employs the same spectral kernel \mathcal{K} for all pixels, changing only the color kernel $C_{i,j}^{I, \sigma_c}$, computed via the same formula at all locations. Instead, we allow each pixel to have a unique spectral kernel $\mathcal{K}_{i,j}$, with weights that can differ significantly between locations based on feedback from a perceptual metric that determines their visual importance and allows maximizing the destruction at less critical regions. Thus, our filters consist of a set \mathcal{K}^* of local $\mathcal{K}_{i,j}$'s for each (i, j) . We include color kernels to ensure the optimization does not explore unwanted directions that violate vital geometric constraints. While these may be limiting, ignoring them causes unnatural distortions if the differences between neighboring pixels are extremely large, making them essential for better convergence and remedying potential perceptual loss imperfections. When the distances are reasonably large but satisfy the perceptual loss with high confidence, it will assign larger weights that counteract the color kernel. Only when these distances are extremely large do they become prohibitive, which is ideal. Hence, our optimizable filter is:

$$\forall I : OF_{\mathcal{K}^*, \mathcal{R}, \sigma_c}(I) = \sum_{m,n} PE_{M \times N}(I) \odot \mathcal{V}^{\mathcal{R}, \mathcal{K}^*, \sigma_c} \quad (4)$$

\mathcal{R} is a reference image for obtaining the color kernels, always chosen as $\mathcal{R} = x_w$. Next, we show how to learn \mathcal{K}^* 's weights.

5.2.3 Adversarial Filtering. Let $\{t \in [T] \mid OF_{\mathcal{K}_t^*, x_w, \sigma_{c_t}}\}$ a series of T optimizable filters (with color kernels computed using x_w), each with their permissiveness and size. We define the composition $\prod_{OF}^T \equiv OF_{\mathcal{K}_1^*, x_w, \sigma_{c_1}} \circ OF_{\mathcal{K}_2^*, x_w, \sigma_{c_2}} \circ \dots \circ OF_{\mathcal{K}_T^*, x_w, \sigma_{c_T}}$. Let ℓ_d be a perceptual loss, t_{ℓ_d} a similarity threshold, and ℓ_F the chosen low-frequency loss. We instantiate eq. (1) to maximize ℓ_F as follows:

$$x_{nw} = \underset{\{\theta_{\mathcal{K}_t^*}\}, \delta}{\operatorname{argmax}} [\ell_F(x_w, \prod_{OF}^T (x_w + \delta))] \quad (5)$$

$$s.t. \ell_d(x_w, \prod_{OF}^T (x_w + \delta)) \leq t_{\ell_d}$$

where $\theta_{\mathcal{K}_t^*}$ are the kernels' weights and δ is a modifier that directly optimizes x_w , similar to eq. (2). We maximize the spectral loss by sequentially propagating the input through a network of filters. Recall that direct modifications are not effective for disrupting low frequencies in the absence of filters due to their inclination to cause high-frequency disturbances only rather than systemic shifts in the

values of many neighboring pixels in a uniform or gradual manner—see §5.2. Thanks to their convolutional nature, this no longer holds with our filters, making their outputs combinations of neighboring pixels. We still include δ that directly manipulates the input despite its inefficacy in the absence of filters. This is because the originally high-frequency disturbances caused by such modifications will now be distributed over neighbors of the receiving pixels due to our filters, translating them into useful low-frequency noise, causing further disruptions beyond the filters' independent ability. Finally, we employ multiple (T) filters stacked after one another. The reason is that chaining several filters with various kernel sizes (geometries) targets different directions and slopes where the watermark could have been injected since watermarking is content-dependent and not all images can be changed similarly.

5.2.4 Spectral Loss. The former DFL is unsuitable for low frequencies (see §5.2) as it fails to force the changes to spread throughout the image. The collective energy at higher frequencies is much smaller in comparison, significantly reducing the total number of pixels that need to change to erase watermarks in these bands, which is achievable without violating the perceptual distance constraints. In contrast, sufficiently manipulating lower frequencies can rapidly change the structure, hindering convergence to an optimal solution if the distortion budget is not carefully distributed. This loss should also ensure our kernels indeed perform the filtering operation, which DFL fails to enforce. Better alternatives are:

Filter Regularization Loss (FRL): This loss enforces that our kernels perform the desired “smoothing” (filtering) and is given as:

$$\forall x \in \mathbb{R}^{Q \times R} : FRL(x) = - \sum_{t \in [T]} FRL_t(x)$$

$$s.t. \forall t : FRL_t(x) = \|x - \mu_{\frac{1}{2}}(x)^{M_t \times N_t}\|_2$$

where $M_t \times N_t$ is the size of our t^{th} kernel \mathcal{K}_t^* and $\mu_{\frac{1}{2}}(x)^{M_t \times N_t}$ computes, for each pixel, the median value of this $M_t \times N_t$ vicinity around it. Maximizing FRL minimizes FRL_t for each filter t , which is the sum of all pixels' distances from the median values in the filter's environment around them in the output, bringing them as close as possible to these local medians. This eliminates variations to the extent possible under the perceptual loss, leading to smoother outputs. As the watermark should be distributed throughout the image, each patch will exhibit increased yet gradual “watermarking”

variations that will be lost when bringing the values closer to these medians. A major benefit of *FRL* is also output consistency.

Mean Pool Loss (MPL): *FRL* is insufficient, as it only ensures proximity of the pixels to the local medians but imposes no constraints on these medians. The *means* of the various patches in the *watermarked* image are highly influenced by the watermark that causes many pixels to change their values. Due to the perceptual loss that strives to retain information, the procedure may converge to a sub-optimal solution, skewing these medians toward the original *means* and only slightly affecting pixel intensities, thereby retaining many of the shifts associated with the watermark. Thus, we require *MPL*:

$$\forall x, y \in \mathbb{R}^{Q \times R}: \quad MPL^{L \times P}(x, y) = \|\bar{x}^{L \times P} - \bar{y}^{L \times P}\|_1$$

$\bar{x}^{L \times P}$ denotes mean pooling with an $L \times P$ window. *MPL* takes the means over each $L \times P$ patch in both inputs and calculates the ℓ_1 difference. As most pixels do not encode watermark information, maximizing the means' differences (w.r.t. the watermarked image) while demanding proximity to the medians (using *FRL*) primarily affects pixels located farther away (those that encode the watermark) from all others, bringing them closer to the rest and eliminating watermarking variations. Additionally, proper low-frequency loss must spread the changes over multiple regions (see §5.2.4). *MPL* does so by dividing the image into patches and demanding that each receive a portion of the change, implying the number of patches must be large. Yet, each must contain enough pixels to manipulate low frequencies. We choose $MPL^{5 \times 5}$ as a compromise, balancing these requirements. Calculating *MPL* for all filter sizes similar to *FRL* is less desirable as when the sizes shift away from this sweet spot, one of the conditions is violated. Note that, without *FRL*, *MPL* is insufficient as it can trivially lead to all pixels in each patch receiving a similar modification ϵ , simply changing the patch's brightness. This behavior satisfies the desired perceptual similarity but leaves the spectrum unaffected as the pixel variation rates remain identical.

5.2.5 Final Low-Frequency Destruction Procedure. (for semantic watermarks) We replace eq. (5)'s abstractions with the above components and *DVL* as the perceptual loss (see §5.1). We also use $\|\cdot\|_2$ regularization to avoid drastic updates and encourage low-frequency, gradual changes. Yet, it is multiplied by a small coefficient to only regulate the process without further influencing the outputs, leaving this to *DVL*. Defining $x_w^{OF_T, \delta} \equiv \prod_{OF} (x_w + \delta)$, we have:

$$x_{nw} = \underset{\{\theta_{K^*}^*, \delta\}}{\operatorname{argmin}} \left[\begin{aligned} &c_{\ell_{DVL}} \cdot \operatorname{ReLU}_{\ell_{DVL}}(x_w, x_w^{OF_T, \delta}) + \lambda_{\|\cdot\|_2} \cdot \|x_w^{OF_T, \delta} - x_w\|_2 \\ &- MPL^{5 \times 5}(x_w, x_w^{OF_T, \delta}) - \lambda_{FRL} \cdot FRL(x_w^{OF_T, \delta}) \end{aligned} \right] \quad (6)$$

We maximize the low-frequency loss $\ell_F = MPL^{5 \times 5} + \lambda_{FRL} \cdot FRL$ by minimizing its negation similar to §5.1. $\operatorname{ReLU}_{\ell_{DVL}}$ ensures visual similarity, keeping the *DVL* distance from x_w below $t_{\ell_{DVL}}$. The resulting changes are gradual, obtained by applying our filters, whose weights are learned to ensure this behavior due to our spectral loss, yielding optimal $\{\hat{\theta}_{K^*}^*, \hat{\delta}\}$ s.t. the final solution is $x_{nw} = x_w^{OF_T, \delta}$, where OF_T denotes the filters applied using $\{\hat{\theta}_{K^*}^*\}$. As each kernel's values should be non-negative and sum to 1, we apply *Softmax* to the learned weights to obtain effective values in this range. λ_{FRL} balances *FRL* and *MPL* and is calibrated s.t. both are simultaneously optimized, while $\lambda_{\|\cdot\|_2}$ limits the impact of the $\|\cdot\|_2$ regularization.

$c_{\ell_{DVL}}$ balances the spectral and visual losses and is determined via a binary search, as in §5.1. We found a single filter network architecture universally effective. Hyperparameter details are in A.3.

Discussion: In the absence of our filters, the modifications at each step are less systemic, allowing different pixels to receive significant updates in opposing directions. Thus, the process will converge to a sub-optimal solution since massive changes that a *subset* of the pixels receive will substantially increase the visual loss, preventing further progress. While our low-frequency loss discourages this behavior and encourages uniform updates, it remains lacking as it is constantly countered by the visual loss that strives to retain similarity from a human's perspective, limiting the number of pixels allowed to change their values, deeming such structural modifications less desirable compared to high-frequency changes that affect a discrete set of pixels thereby remaining potentially unnoticeable. Our filters, however, force the procedure to prioritize collective updates, drastically improving its performance. Readers are referred to A.5 for empirical results that establish these benefits.

This also explains why this attack, while effective against *semantic* watermarks, is unsuitable for removing *non-semantic* ones (see §6.2.2). The reason is that our low-frequency loss and filters encourage low-magnitude, yet collective, modifications and prevent significant updates to specific pixels (as opposed to §5.1). Yet, *non-semantic* watermarks are injected in high frequencies and thus rely on large variations between neighboring pixels. As this process can only slightly affect such peaks, the watermark will be preserved.

6 EXPERIMENTS

6.1 Setup

Schemes. We experiment with seven *SOTA* schemes listed in Table 1 that cover the categories discussed in §2. They were selected since they recently appeared in top venues, and several of them remain unbroken by a *query-free black-box* attacker. Among the *generator-specific* schemes, the evaluated (original) implementations of *Yu1* [66], *Yu2* [65], and *PTW* [46] watermark GANs [24], while *StableSignature* [22] and *TRW* [63] operate on *LDMs* [52] (see A.1 for details on synthesis algorithms). We are not aware of *semantic* schemes that appeared in top venues other than those we consider, which have also been the focus of previous works [8, 53, 71]. As most recent schemes are *generator-specific*, we include five such algorithms compared to two *general-purpose* systems.

Table 1: The *SOTA* schemes we study.

	General-Purpose	Generator-Specific
Semantic	StegaStamp [60]	TRW [63]
Non-Semantic	HiDDeN [74]	Yu1 [66], Yu2 [65], PTW [46], StableSignature [22]

Data. Most *generator-specific* schemes require no data, generating random images. Yet, as *TRW* and *StableSignature* watermark text-to-image *LDMs* (*StableDiffusion* [4]), we use prompts from *Stable Diffusion*'s test set. For *HiDDeN*, we use test samples from the *COCO* dataset [43] on which it was trained. *StegaStamp* watermarks 400×400 images. Thus, we downscale samples from the known *CelebA-HQ-1024* [35]². We evaluate each system on 100 random images, similar to previous work [34].

²FFHQ-1024 [37] samples yield similar results. For brevity, we focus on CelebA-HQ.

Metrics. Removing a watermark entails satisfying two conditions: 1) It must no longer be detected, and 2) the output should retain quality and proximity to the watermarked image (see §3).

Detection: For binary watermarks, detection occurs if the ratio of bits matching the watermark in the sequence extracted from the image is above some threshold t_w . As in previous work [45, 71], we select t_w that can reject the null hypothesis H_0 that k or more matching bits were randomly extracted with $p < 0.01$. This has probability $P(X \geq k | H_0) = \sum_{i=k}^n \binom{n}{i} 0.5^n$, for watermark length n . Thus, $t_w = \frac{k}{n}$ for which this probability is below 0.01 is selected. We denote the portion of successfully extracted bits as the *bit accuracy*, which we compare against t_w . Watermark lengths are in A.2. *TRW*’s watermarks are unbounded, and detection occurs if the ℓ_1 distance—or effectively, the *Mean Absolute Error (MAE)*—of the extracted sequence from the watermark is below a threshold determined s.t. the ratio of falsely detected non-watermarked images (*FPR*) is low. We chose a higher *FPR* (0.02) than the original paper [63] (0.01), making the attacker’s task harder, arriving at $MAE = 71$. For consistency with other schemes, we use this distance’s *inverse*: for the watermark to be detected, the *MAE*’s *inverse* must be $\geq t_w = \frac{1}{71}$.

Quality: We use two metrics common in previous work [8, 22, 32, 45, 46, 71]: Learned Perceptual Similarity (*LPIPS* [69]) and *Fr chet Inception Distance (FID)* [29]. To eliminate biases, we refrain from using the *LPIPS* methods *UnMarker* employs (see §5.1) as our attacks explicitly optimize these metrics. Instead, we use well-known *LPIPS-VGG* [69]. *FID* evaluates the attack samples’ distributions w.r.t. the datasets of watermarked images, measuring *dataset-wise* similarity.

Baselines. We include various typical manipulations. Their parameters were chosen following previous work [46, 71] and to allow maximum distortion while retaining acceptable quality. These are *Mild Center Cropping*, *JPEG compression*, *Quantization*, and *Gaussian Blurring* (filtering) with a 5×5 kernel. We also evaluate *Guided Blurring* to demonstrate how even these stronger filters cannot break robust watermarks, as argued in §5.2. Their kernel size is also 5×5, but we exploit their edge-preserving properties to increase its *std.* (to 5.0). To control the modulation at edges, these accept an additional *color kernel’s std.* (see §5.2), for which we have three values: 0.1, 1.0, and 5.0. Yet, 1.0 and 5.0 are overly destructive and do not preserve quality, chosen only to better explore robustness. We also evaluate *UnMarker* against the *SOTA DiffusionAttack* [8, 53, 71] and *VAEAttack* [8, 71]. To our knowledge, these regeneration techniques are the only existing practical (*black-box* and *query-free*) and effective attacks, as adversarial attacks make unrealistic relaxing assumptions (see §2) and are therefore disqualified.

6.2 Evaluations

6.2.1 Watermark Utility. First, we ensure the chosen schemes’ utility, following the requirements from §4.1: *Applicability*, *Stealthiness*, and *Robustness to Manipulations*. While the latter demands withstanding basic manipulations, true robustness is contingent on resisting advanced attacks as well. We separate these cases for consistency with watermark papers that mainly consider standard manipulations. Stronger attacks are in §6.2.3. We focus on *Applicability* and *Robustness* since we use original implementations of *SOTA* systems whose *stealthiness* has been shown by their authors.

Visual metrics are excluded here, as evaluating the naive manipulations’ output quality is not our objective, knowing that our *basic* settings are quality-preserving [46, 71]. We do not evaluate the rotation manipulations by Zhao et al. [71], following their arguments w.r.t. their impracticality as they can be easily spotted and corrected before invoking the detector. Still, their finding of some of the more robust schemes being vulnerable to rotations may seem to contradict our assertions in §4.1 that these watermarks are in the spectral amplitudes as such watermarks should remain unaffected by rotations that preserve these magnitudes. Indeed, some schemes were found agnostic to rotations. As for the systems exhibiting this vulnerability, note that watermarking schemes are generally not **explicitly designed** to construct watermarks in the spectral amplitudes. Rather, this behavior is naturally adopted when trained for robustness to various practical manipulations (see §4). Failure to expose these systems to a wider set of demands during training (e.g., resistance to rotations) may result in them mistakenly associating **additional** indicators, such as a specific image orientation, with the watermark. Yet, as rotations are impractical, this is not an issue.

A detailed analysis is deferred to A.4 alongside the results (Table 5). All schemes behave as desired without manipulations, detecting watermarked images: For binary watermarks, the *bit accuracies* are far above the thresholds, approaching 100%. For *TRW*, the *inverse distance* is 0.022, well over the 0.0141 threshold. All systems are fairly resistant to manipulations. *Semantic* schemes remain almost unaffected. Among *non-semantic* schemes, *Yu1* and *StableSignature* are the most resistant, retaining robustness against all *realistic* configurations. Yet, the latter shows some vulnerability to *Guided Blurring* with overly destructive parameters (*color std.* ≥ 1.0), but since this is not a practical attack, it remains reliable. *PTW* rejects most manipulations but is affected by reasonable *Quantization* (10), while the less advanced *HiDDeN* is vulnerable to *JPEG* and *Blurring*. *Yu2* resists all manipulations except *cropping*, indicating high dependency on spatial attributes, making it unsuitable for watermarking, as it violates the *robustness* requirement from §4.1.

The results demonstrate how all schemes aside from *Yu2* are robust to spatial manipulations such as *cropping*, indicating their watermarks reside in a different channel, which we know and will next verify empirically is the spectral amplitudes. This is evident for *PTW* and *HiDDeN* that exhibit vulnerability to *Quantization* and *JPEG* that affect high frequencies. The resistance of other schemes to these manipulations, however, does not imply robustness but rather that their watermarks are harder to remove. Yet, advanced attackers can still break these systems, as we show below. *Yu2* is highly dependent on information encoded in the background’s pixels, suggesting its watermarks are not constructed as robust, collective measurements but rather in volatile spatial locations.

6.2.2 UnMarker. We now evaluate *UnMarker*’s ability to universally remove watermarks. In §6.2.3, we compare *UnMarker* to *SOTA* attacks and assess its capability of preserving visual similarity.

Configuration. Our analyses and experiments above prove that a conventionally robust scheme (under spatial manipulations) must inject its watermarks in the frequency space since naive manipulations (e.g., *cropping*) severely impact spatial watermarks that are forced to primarily reside in the background. Schemes that are spatial in nature and therefore rely less on spectral watermarking

Table 2: Performance of watermarking schemes against each stage of *UnMarker*. The complete attack is in the last row (*CHL*). Numbers in parentheses are the detection thresholds, while *Detect* is the portion of images meeting them.

Scheme		Yu1 (61%)		Yu2 (63%)		HiDDeN (73%)		PTW (70%)		StableSignature (69%)		StegaStamp (63%)		TRW (0.0141)	
Attack		Bit Acc↓	Detect↓	Bit Acc↓	Detect↓	Bit Acc↓	Detect↓	Bit Acc↓	Detect↓	Bit Acc↓	Detect↓	Bit Acc↓	Detect↓	Inv. Dist.↓	Detect↓
UnMarker	CH	59.04%	33%	53.06%	0%	58.34%	1%	63.11%	11%	53.08%	4%	94.87%	100%	0.0152	99%
	CL	73.16%	100%	54.62%	0%	84.21%	98%	95.21%	100%	97.6%	100%	61.8%	43%	0.0141	55%
	HL	73.11%	100%	99.23%	100%	72.28%	66%	61.53%	6%	54.59%	9%	64.64%	59%	0.016	98%
	CHL	59.08%	31%	53.03%	0%	58%	0%	62.75%	11%	52.82%	4%	61.49%	43%	0.014	40%

(e.g., *Yu2*) may hence evade *UnMarker*’s spectral optimizations as they are not designed to target these inherently fragile schemes. Yet, equipping *UnMarker* with a simple *cropping* layer suffices to defeat such weaker systems. Moreover, as spectral watermarks distribute their modifications throughout the image to minimize visual cues (see §4), *cropping* also can slightly “weaken” those by eliminating partial modifications residing in the background. This allows using a decreased distortion budget for the optimization stages.

Thus, *UnMarker*’s design is as follows: We apply mild *cropping*, followed by high-frequency destructive optimizations (§5.1). Finally, our filtering-based stage (§5.2) eliminates low-frequency traces. This yields a comprehensive attack that targets all *carriers*, erasing all watermarks. Attackers can adjust the *cropping* ratio to restrict the output to the actual content. For our experiments, 10% perfectly retains the content. The stages’ order does not affect the results.

While *UnMarker* relies on several hyperparameters, they should all be calibrated to maximize the spectral loss regardless of the system under attack, complying with our threat model. Instead, they are only affected by properties of the image, such as its size, which, we found to be the only relevant factor. The hyperparameters are in A.3. The size-dependant parameters are merely the thresholds and coefficients. Meanwhile, the number of filters and their kernel sizes are invariant, as by combining multiple filter sizes, a single architecture can defeat any *semantic* watermark (see 5.2).

Results. We report settings combining different stages of *UnMarker*, identifying crucial insights that establish our theory. These configurations are *CH*— the high-frequency destructive process preceded by *cropping*, *CL*— the low-frequency optimization (with *cropping*), *HL*— the two optimizations without *cropping*, and *CHL*, denoting the full *UnMarker* with all three stages. Results are in Table 2.

Non-Semantic Schemes. Robust non-semantic schemes (w.r.t. known manipulations) cannot alter the content and thus must embed their watermarks in high frequencies. Hence, minimal disruptions to this part of the spectrum where the energy concentration is low suffices to remove them. Our results corroborate this as all such schemes break under *CH* that combines *cropping* and high-frequency disruptions. The detection rates of the *conventionally* robust algorithms (that resist *cropping*— all but *Yu2*) remain almost unaffected by *CL*, which primarily targets low frequencies where they do not operate. *Yu2* is defeated by *CH*, but *HL*’s results prove this is not due to our optimization since the scheme is insensitive to manipulations in both parts of the spectrum, indicating that *cropping* only is responsible for this outcome. This comes as no surprise since *Yu2* employs *spatial* watermarking that enables it to resist spectral optimizations but makes it trivially vulnerable to *cropping*.

While schemes that process larger images (*PTW* and *StableSignature*) are almost insensitive to *cropping* (see Table 5), they are extremely vulnerable to high-frequency manipulations, evident by

their robustness to *CL* and fragility against *HL*, bringing their detection to 6% and 9%, respectively. *Yu1* and *HiDeN* that watermark smaller 128×128 images retain 100% detection even against *HL*. Yet, their *bit accuracies* drop sharply from 98.42% and 99.16% (Table 5) to 73.11% and 72.28%. The cause for this decline is our high-frequency destruction since *CL* that combines *cropping* and low-frequency disruptions offers almost no advantages compared to *cropping*.

Thus, there is a connection between the image size, sensitivity to *cropping*, and vulnerability to high-frequency modifications, which is easy to explain: Spatial *robustness* and *stealthiness* require spreading the watermark across the image. Meanwhile, *non-semantic* watermarks are restricted to specific regions (i.e., edges) where they can exploit the high-frequency nature (see §4.1.1) to remain invisible. As the size shrinks, such areas become less prevalent in central parts, forcing the changes to be delegated to the background and making them more vulnerable to *cropping*. Accordingly, the portion of the change each region receives grows as well, making it difficult to eliminate these watermarks with minimal modifications, explaining why they retain *bit accuracies* above the threshold despite a significant decline without *cropping*. Regardless, *cropping* then becomes capable of eliminating sufficient footprints to further decrease these values below the thresholds, as seen for *CH* (*CHL*).

Increasing the size enables schemes to better reject *cropping* since this new-found resolution creates opportunities for embedding the watermark in central areas. However, the footprint in these regions must be significantly smaller. Thus, minute high-frequency disruptions throughout the image become far more effective, explaining their inability to withstand our high-frequency optimizations alone.

***UnMarker* (*CHL*) breaks all non-semantic schemes, with the most resistant being *Yu1* that retains a detection rate of 31%. Yet, this is worse than a random guess, leaving it useless. Semantic Schemes.** Both *StegaStamp* and *TRW* are resistant to high-frequency disruptions, with their detection rates fixed at 100% for *CH* and the *bit accuracies* for *StegaStamp* and *inverse distances* for *TRW* retaining almost identical values to those observed when only *cropping* is applied. Yet, both are extremely vulnerable to low-frequency disruptions, evident by their significant performance decline against *CL*: *StegaStamp*’s detection drops to 43% while *TRW*’s becomes 55%. This cements our arguments regarding *semantic* watermarks being primarily in lower frequencies and the soundness of our filtering-based approach. When comparing *CL* to the final results (*CHL*), we observe identical results for *StegaStamp*, while *TRW* exhibits an additional decline from 55% to 40%, indicating that a small portion of its watermarks is at higher frequencies.

StegaStamp’s watermarks are more visible (see §2.1), allowing them to be engraved in the *main* content, and increasing their robustness to spatial manipulations (*cropping*). Since *TRW* produces less visible watermarks despite targeting low frequencies where

Table 3: Comparison with SOTA attacks. For each metric, bold entries correspond to the best attack against the relevant scheme. Gray cells denote scores meeting our quality and complete removal criteria for *LPIPS* (0.15) and *Detect* (50%), respectively.

Attack	Scheme	Yu1 (61%)				Yu2 (63%)				HiDDeN (73%)				PTW (70%)				StableSignature (69%)				StegaStamp (63%)				TRW (0.0141)			
		FID↓	LPIPS↓	Bit Acc↓	Detect↓	FID↓	LPIPS↓	Bit Acc↓	Detect↓	FID↓	LPIPS↓	Bit Acc↓	Detect↓	FID↓	LPIPS↓	Bit Acc↓	Detect↓	FID↓	LPIPS↓	Bit Acc↓	Detect↓	FID↓	LPIPS↓	Bit Acc↓	Detect↓	FID↓	LPIPS↓	Inv. Dist.↓	Detect↓
UnMarker	(CHL)	34.07	0.15	59.08%	31%	22.88	0.1	53.03%	0%	39.56	0.08	58%	0%	11.9	0.14	62.75%	11%	30.87	0.05	52.82%	4%	34.69	0.08	61.49%	43%	60.73	0.1	0.014	40%
Diffusion Attack	no cropping	12.38	0.2	58.31%	28%	13.09	0.17	68.29%	87%	34.1	0.18	59.8%	3%	22.95	0.26	55.53%	7%	36.57	0.32	47.89%	0%	33.15	0.36	83.21%	100%	41.69	0.32	0.0155	99%
	+cropping	14.02	0.18	54.24%	8%	11.98	0.17	51.26%	3%	36.97	0.19	56.61%	0%	19.98	0.25	62.01%	16%	41.88	0.31	47.78%	0%	30.83	0.33	77.84%	95%	41.16	0.31	0.0144	79%
VAE Attack	quality=3	36.2	0.15	67.19%	97%	19.67	0.13	73.89%	96%	65.16	0.22	60.4%	8%	26.6	0.26	73.63%	89%	72.21	0.37	48.25%	0%	54.89	0.42	97.9%	100%	71.91	0.38	0.0154	90%
	quality=2	46.82	0.18	64.42%	81%	27.4	0.16	66.62%	78%	83.4	0.26	58.36%	1%	39.11	0.29	71.33%	79%	94.85	0.41	44.93%	0%	70.86	0.46	94.7%	100%	93.56	0.41	0.015	88%
	quality=1	58.37	0.22	60.63%	59%	38.9	0.19	61%	36%	104.92	0.32	56.26%	2%	54.93	0.33	66.74%	36%	128.88	0.44	43.87%	0%	87.8	0.49	88.84%	100%	118.85	0.46	0.0145	67%

significant watermarking footprints are required, it behaves similar to *non-semantic* schemes for small images, forcing a considerable portion of these changes to populate the background. The results for *cropping* (Table 5), *CL*, *CH* and *CHL* (Table 2) prove this; while *cropping* has minimal effects on *StegaStamp* (the *bit accuracy* only drops to 93.96%), *TRW* is more sensitive as its *inverse distance* decreases from 0.022 to 0.155 when the threshold is only 0.0141. Although this is in the detection range, combining *cropping* with *UnMarker*’s low-frequency disruptions (*CL*, *CHL*) erases its watermarks.

While *TRW*’s *inverse distance* is drastically lowered by spectral optimizations (*HL*), bringing it down to 0.016 from 0.022, they do not erase its watermarks, unlike *StegaStamp*’s. This is because low-frequency distortions affect many pixels simultaneously. Hence, under a strict budget, the number of regions in which these rates can be altered is limited compared to high-frequencies. Thus, *StegaStamp*, whose watermarks are more concentrated, requires fewer areas to be modified, leading to the optimization being successful without *cropping*. Yet, we verified that low-frequency disruptions with a higher budget or number of steps eventually break *TRW* without *cropping*. However, this may introduce unwanted artifacts unless carefully done. *Cropping* is as effective but less demanding.

UnMarker defeats all studied systems due to the irremediable trade-offs of defensive watermarking, as making watermarks robust to spatial manipulations leaves them vulnerable to spectral disruptions and vice versa. Even when failing to bring the detection to 0%, it leaves the scheme useless, with a probability below a random guess.

6.2.3 Comparison with SOTA attacks. Here, we compare *UnMarker* to regeneration attacks—the *VAEAttack* [8, 71] and *DiffusionAttack* [8, 53, 71]. Despite being certifiably guaranteed to remove *non-semantic* watermarks, they fail against *semantic* methods. This robustness creates a false sense of security around *semantic* watermarks [8, 71], which *UnMarker* disproves. Additionally, the guarantees ensure *non-semantic* watermarks will be removed if the attacks introduce sufficient noise into the image, followed by a denoising process to restore it without the watermark that has now been diluted. Stronger watermarks require increased perturbations that prevent perfect reconstruction. Unnatural artifacts can be avoided by using advanced regeneration systems, explaining why the more sophisticated *DMs* perform better, as they can apply larger distortions while still somewhat accurately retrieving the content, as opposed to off-the-shelf *VAEs*. Yet, the similarity to the original image may still be lost under such large budgets. *UnMarker* eliminates all these hurdles, significantly decreasing the distortion while being effective even against the stronger *semantic* schemes.

Since *UnMarker* uses *cropping*, we apply the *DiffusionAttack* with and without *cropping* for a fair comparison. The *VAEAttack*’s image quality was deemed inferior, disqualifying many of its results (see below), and thus a similar comparison was excluded. Results are in Table 3, and samples produced by the three attacks are in A.6.

Visual Quality and Similarity: The range for *LPIPS* is [0, 1]. Images with *LPIPS* distance at the 0.1 level (i.e., well below 0.2) are visually similar [26]. Thus, we choose 0.15 as a cut-off beyond which we say the attack begins to cause visible changes. This does not mean that slightly higher scores will lead to severe quality degradation since the changes may integrate well with the content. Yet, scores far beyond this threshold attest to the poor nature of the outputs. Despite *FID*’s known ability to measure similarity, it suffers from two major shortcomings: first, it compares the *datasets* of watermarked images and those that have undergone the attack and cannot judge samples on an image-by-image basis. Moreover, it may exhibit inconsistencies with human vision, making it less ideal in certain instances [44]. Thus, while *FID* is important for assessing quality, we prioritize *LPIPS* as it can better provide fine-grained judgments.

We do not consider the *VAEAttack* effective. It allows choosing from eight quality options that control the added noise before regeneration. We apply it with the three lowest options, as we found increasing this factor beyond 3 makes the attack almost always ineffective. However, all three options severely impact the quality, invalidating the attack. This can be seen in Table 3, as both its *FID* and *LPIPS* are extremely worse (larger) than the other attacks whenever it degrades the detection rates. For larger images (over 256×256), even the best factor (3) is destructive, resulting in *LPIPS* scores at least 3.8x compared to *UnMarker* and far above the 0.15 cut-off. Its *FIDs* are also inflated. While its *FID* against *TRW* (71.91) is close *UnMarker*’s (60.73), its *LPIPS* is extremely worse, indicating low quality. For smaller images, it retains similarity for *Yu1*, *Yu2* and *PTW* with *quality* = 3, but fails to remove their watermarks. *HiDDeN*’s watermarks are removed with this factor at an acceptable *LPIPS* (0.22). Still, the failure against all other systems limits this attack’s potential. Lowering the factor impacts quality, invalidating any results for larger images (including *PTW*). For *Yu1* and *Yu2*, as the attack fails to achieve remarkable removal for *quality* = 2, the only relevant case is *quality* = 1. The two systems retain acceptable *LPIPS* scores (0.22 and 0.19) but violate the 0.15 threshold, and their *FID* scores are far worse than the other attacks, proving the *VAEAttack* fails to preserve quality even for these systems (see A.6).

The *DiffusionAttack* is controlled via a parameter *t*. Following Saberi et al. [53], *t* > 0.2 causes significant deviations from the watermarked input, invalidating the attack. We found that for smaller images (128×128), this occurs at much lower values. For

these images, we set $t = 0.05$ as we deemed it the turning point. Lowering t beyond the chosen values results in less successful attacks. *UnMarker* always achieves better *LPIPS*. The differences become drastic for larger images (over 256×256)—0.1 at most for *UnMarker* compared to ≥ 0.37 for the *DiffusionAttack*. *UnMarker*'s *LPIPS* scores are 0.15 at most, ensuring indistinguishability from the watermarked content. In contrast, the higher scores obtained by the *DiffusionAttack*, while not necessarily indicating significant deviations, inevitably entail that some nuances between the image pairs will appear, which may lead to the attack samples being identified as fake, as can be seen in A.6. The attacks' *FIDs* alternate, outperforming one another against different schemes. Yet, both attain far better scores than the *VAEAttack*'s, proving its inferiority.

***UnMarker* attains the lowest *LPIPS*, with its worst score being 0.15, ensuring resemblance to the watermarked images. The similarity between *UnMarker*'s *FIDs* and the *DiffusionAttack*'s, which was previously shown to produce high-quality outputs [71], further establishes *UnMarker*'s quality.**

Watermark Removal: An attack *completely* removes watermarks if it brings the detection to 50% or below, as the scheme becomes of no use. Both baselines remove *non-semantic* watermarks, although the *VAEAttack*'s quality degradation invalidates its results. *UnMarker* always outperforms this attack except against *StableSignature* for which *UnMarker* brings the detection to 4% while the *VAEAttack* reduces it to 0%. Still, this difference is insignificant. The *DiffusionAttack* and *UnMarker* obtain similar results on average, but the *DiffusionAttack* (+*cropping*) significantly outperforms *UnMarker* against *Yu1*, reducing its detection to 8% compared to 31%. Yet, as both drive this rate below 50%, specific numbers are irrelevant.

Our results validate the baselines' known inability to remove *semantic* watermarks [8, 53, 71]. The *VAEAttack* is moderately successful against *TRW*, especially with quality 1, bringing its detection to 67%, but, as explained above, we do not consider it valid. The *DiffusionAttack* leaves both detection rates almost unchanged despite reducing *StegaStamp*'s *bit accuracy* and *TRW*'s *inverse distance* from 99.95% and 0.022 to 83.21% and 0.0155. While *cropping* decreases these numbers slightly to 77.84% and 0.0144 and makes the attack more successful against *TRW*—79% detection, *UnMarker* drastically outperforms it, reducing this rate to 40% and *StegaStamp*'s, against which the *DiffusionAttack* is ineffective, to 43%.

Overall, among the two baselines, only the *DiffusionAttack* can remove watermarks without violating visual constraints. Yet, ***UnMarker* remains far superior as it succeeds against *semantic* watermarks where the *DiffusionAttack* fails.**

7 DISCUSSION

Practicality. *UnMarker* can be executed offline as it requires no detector interaction, given only the watermarked image. A single attack takes up to 5 minutes with a 40GB A100 GPU. Such machines are available for \$32.77/hr on AWS [1], making it highly practical.

Existing query-free black-box attacks (see §6.2.3) require advanced denoising pipelines (e.g., VAEs and DMs), whose ability to preserve quality depends on their computational power and the commonalities between their training data and the distributions from which watermarked images are generated and fail when these conditions are not met as we demonstrated for the *VAEAttack*. While

the *DiffusionAttack* achieves better quality (despite it being inferior to *UnMarker*'s), the DM [4] used in this attack and all the studied schemes were trained on public datasets. In practice, providers possess exclusive high-quality data, which may vary significantly from those used to train the DMs available to the attacker. Thus, the *DiffusionAttack* may incur significant quality degradation in reality. *UnMarker*'s data-free nature is agnostic to these nuances.

Mitigations. *UnMarker* erases the watermark's footprint. Although it is an adversarial attack, known mitigations (e.g., *adversarial training* [8, 32, 61]) are not applicable since, in our unique scenario, *UnMarker* itself **removes** an "adversarial" signature (i.e., the watermark) previously injected by the provider. This volatility of watermarks (being adversarial themselves) makes them a weak attestation method: once these fragile signatures are removed, they cannot be restored. This is in contrast to traditional adversarial problems wherein the true class of the sample is retained and may be recovered by discarding the attacker's minor modifications. Hence, watermark removal cannot evolve into a cat-and-mouse game where providers continue to devise defenses. *UnMarker*'s persistence comes from its destructive nature and its agnosticism of the target scheme. On the other hand, known *adversarial* attacks against defensive watermarking [34, 45, 53] follow "traditional" principles, relying on *detector feedback* to generate disruptions by exploiting its imperfections, yielding "volatile" adversarial samples lying in uncertainty regions of these systems. This makes them reversible via adversarial defenses, as they may *retain* the watermark but overshadow it with bounded noise that can be eliminated. Our findings indicate that watermarking is not a viable defense against deepfakes and urge the community to explore alternatives.

Ethical Considerations. Misusing *GenAI* can have severe impacts on society. Our attack does not aim to help generate harmful content but to raise awareness regarding these systems' risks. Although we are not aware of providers that have already rolled out stable watermarking algorithms, the pace at which they are being adopted, and the attention from entities such as the *White House* that has secured commitments from providers to deploy these solutions [28] make it mandatory that they are thoroughly assessed. While we reached out to providers requesting access to their APIs for evaluation, we never heard back. Thus, all our studied systems (including Facebook Research's *StableSignature* [22]) are open-source.

8 CONCLUSION

We presented a novel attack against defensive watermarking via adversarial optimizations that disrupt the spectra of watermarked images and interfere with the watermarks' footprints, erasing them without interacting with the scheme. *UnMarker* is effective against all systems, including *semantic* schemes that have been assumed robust to such *query-free* and *black-box* attacks. Our results expose the risks associated with defensive watermarking and urge providers to invest further efforts in developing more robust deepfake defenses.

ACKNOWLEDGMENTS

We gratefully acknowledge the support of the Waterloo-Huawei Joint Innovation Laboratory for funding this research, and the Compute Canada Foundation (CCF) for their resources that made our experiments possible.

REFERENCES

- [1] [n. d.]. Cloud computing services - Amazon Web Services (AWS). <https://aws.amazon.com>.
- [2] [n. d.]. DALL-E 2. <https://openai.com/dall-e-2>.
- [3] [n. d.]. Stability AI. <https://stability.ai/>.
- [4] [n. d.]. stabilityai/stable-diffusion-2-1. <https://huggingface.co/stabilityai/stable-diffusion-2-1>.
- [5] [n. d.]. Stable diffusion API. https://clipdrop.co/stable-diffusion?utm_campaign=stable_diffusion_promo.
- [6] [n. d.]. What is Generative AI and what are its applications? <https://cloud.google.com/use-cases/generative-ai>.
- [7] Shruti Agarwal, Hany Farid, Yuming Gu, Mingming He, Koki Nagano, and Hao Li. 2019. Protecting World Leaders Against Deep Fakes. In *CVPR workshops*, Vol. 1. 38.
- [8] Bang An, Mucong Ding, Tahseen Rabbani, Aakriti Agrawal, Yuancheng Xu, Chenghao Deng, Sicheng Zhu, Abdurak Mohamed, Yuxin Wen, Tom Goldstein, et al. 2024. Benchmarking the Robustness of Image Watermarks. *arXiv preprint arXiv:2401.08573* (2024).
- [9] Ashley Belanger. 2023. OpenAI, Google will watermark AI-generated content to hinder deepfakes, misinfo. <https://arstechnica.com/ai/2023/07/openai-google-will-watermark-ai-generated-content-to-hinder-deepfakes-misinfo/>.
- [10] Ning Bi, Qiyu Sun, Daren Huang, Zhihua Yang, and Jiwu Huang. 2007. Robust Image Watermarking Based on Multiband Wavelets and Empirical Mode Decomposition. *IEEE Transactions on Image Processing* 16, 8 (2007), 1956–1966. <https://doi.org/10.1109/TIP.2007.901206>
- [11] Xuwen Cao, Subramanya Rao Dulloor, and Marcella Cindy Prasetyo. 2017. Face generation with conditional generative adversarial networks. *arXiv preprint arXiv:2303.10137*. (2017).
- [12] Xiaoyu Cao and Neil Zhenqiang Gong. 2021. Understanding the security of deepfake detection. In *International Conference on Digital Forensics and Cyber Crime*. Springer, 360–378.
- [13] Han Chen, Yuezun Li, Dongdong Lin, Bin Li, and Junqiang Wu. 2023. Watching the BiG Artifacts: Exposing DeepFake Videos via Bi-Granularity Artifacts. *Pattern Recogn.* 135, C (mar 2023), 11 pages. <https://doi.org/10.1016/j.patcog.2022.109179>
- [14] Ryan Connor. 2023. Modern generative AI for images. <https://www.assemblyai.com/blog/modern-generative-ai-images/>.
- [15] Riccardo Corvi, Davide Cozzolino, Giada Zingarini, Giovanni Poggi, Koki Nagano, and Luisa Verdoliva. 2023. On the detection of synthetic images generated by diffusion models. In *ICASSP 2023-2023 IEEE International Conference on Acoustics, Speech and Signal Processing (ICASSP)*. IEEE, 1–5.
- [16] Dustin T Crystal, Nicholas G Cuccolo, Ahmed Ibrahim, Heather Furnas, and Samuel J Lin. 2020. Photographic and video deepfakes have arrived: how machine learning may influence plastic surgery. *Plastic and reconstructive surgery* 145, 4 (2020), 1079–1086.
- [17] Steffen Czolbe, Oswin Krause, Ingemar Cox, and Christian Igel. 2020. A loss function for generative neural networks based on Watson’s perceptual model. *Advances in Neural Information Processing Systems* 33 (2020), 2051–2061.
- [18] Emilia David and Alex Heath. 2024. Meta says you better disclose your AI fakes or it might just pull them. <https://www.theverge.com/2024/2/6/24062388/meta-ai-photo-watermark-facebook-instagram-threads>.
- [19] Adrienne De Ruiter. 2021. The distinct wrong of deepfakes. *Philosophy & Technology* 34, 4 (2021), 1311–1332.
- [20] Chengdong Dong, Ajay Kumar, and Eryun Liu. 2022. Think Twice Before Detecting GAN-generated Fake Images from their Spectral Domain Imprints. In *2022 IEEE/CVF Conference on Computer Vision and Pattern Recognition (CVPR)*. 7855–7864. <https://doi.org/10.1109/CVPR52688.2022.00771>
- [21] Sandy Engelhardt, Lalith Sharan, Matthias Karck, Raffaele De Simone, and Ivo Wolf. 2019. Cross-domain conditional generative adversarial networks for stereoscopic hyperrealism in surgical training. In *International Conference on Medical Image Computing and Computer-Assisted Intervention*. Springer, 155–163.
- [22] Pierre Fernandez, Guillaume Couairon, Hervé Jégou, Matthijs Douze, and Teddy Furon. 2023. The Stable Signature: Rooting Watermarks in Latent Diffusion Models. *ICCV* (2023).
- [23] Joel Frank, Thorsten Eisenhofer, Lea Schönherr, Asja Fischer, Dorothea Kolossa, and Thorsten Holz. 2020. Leveraging frequency analysis for deep fake image recognition. In *International conference on machine learning*. PMLR, 3247–3258.
- [24] Ian Goodfellow, Jean Pouget-Abadie, Mehdi Mirza, Bing Xu, David Warde-Farley, Sherilj Ozair, Aaron Courville, and Yoshua Bengio. 2014. Generative adversarial nets. *Advances in neural information processing systems* 27 (2014).
- [25] Sven Goyal. 2023. Identifying AI-generated images with Synthid. <https://deepmind.google/discover/blog/identifying-ai-generated-images-with-synthid/>.
- [26] Qingying Hao, Licheng Luo, Steve TK Jan, and Gang Wang. 2021. It’s not what it looks like: Manipulating perceptual hashing based applications. In *Proceedings of the 2021 ACM SIGSAC Conference on Computer and Communications Security*. 69–85.
- [27] Drew Harwell. 2018. Scarlett Johansson on fake AI-generated sex videos: “nothing can stop someone from cutting and pasting my image”. <https://www.washingtonpost.com/technology/2018/12/31/scarlett-johansson-fake-ai-generated-sex-videos-nothing-can-stop-someone-cutting-pasting-my-image/>.
- [28] Melissa Heikkilä. 2023. Google DeepMind has launched a watermarking tool for AI-generated images. <https://www.technologyreview.com/2023/08/29/1078620/google-deepmind-has-launched-a-watermarking-tool-for-ai-generated-images/>.
- [29] Martin Heusel, Hubert Ramsauer, Thomas Unterthiner, Bernhard Nessler, and Sepp Hochreiter. 2017. Gans trained by a two time-scale update rule converge to a local nash equilibrium. *Advances in neural information processing systems* 30 (2017).
- [30] Emmie Hine and Luciano Floridi. 2022. New deepfake regulations in China are a tool for social stability, but at what cost? *Nature Machine Intelligence* 4, 7 (2022), 608–610.
- [31] Shu Hu, Yuezun Li, and Siwei Lyu. 2021. Exposing GAN-generated faces using inconsistent corneal specular highlights. In *ICASSP 2021-2021 IEEE International Conference on Acoustics, Speech and Signal Processing (ICASSP)*. IEEE, 2500–2504.
- [32] Yuepeng Hu, Zhengyuan Jiang, Moyang Guo, and Neil Gong. 2024. A Transfer Attack to Image Watermarks. *arXiv preprint arXiv:2403.15365* (2024).
- [33] Yonghyun Jeong, Doyeon Kim, Seungjai Min, Seongho Joe, Youngjune Gwon, and Jongwon Choi. 2022. BiHPF: Bilateral High-Pass Filters for Robust Deepfake Detection. In *2022 IEEE/CVF Winter Conference on Applications of Computer Vision (WACV)*. 2878–2887. <https://doi.org/10.1109/WACV51458.2022.00293>
- [34] Zhengyuan Jiang, Jinghui Zhang, and Neil Zhenqiang Gong. 2023. Evading Watermark based Detection of AI-Generated Content. In *ACM Conference on Computer and Communications Security (CCS)*.
- [35] Tero Karras, Timo Aila, Samuli Laine, and Jaakko Lehtinen. 2017. Progressive growing of gans for improved quality, stability, and variation. *arXiv preprint arXiv:1710.10196* (2017).
- [36] Tero Karras, Miika Aittala, Samuli Laine, Erik Härkönen, Janne Hellsten, Jaakko Lehtinen, and Timo Aila. 2021. Alias-free generative adversarial networks. *Advances in Neural Information Processing Systems* 34 (2021), 852–863.
- [37] Tero Karras, Samuli Laine, and Timo Aila. 2019. A style-based generator architecture for generative adversarial networks. In *Proceedings of the IEEE/CVF conference on computer vision and pattern recognition*. 4401–4410.
- [38] Tero Karras, Samuli Laine, Miika Aittala, Janne Hellsten, Jaakko Lehtinen, and Timo Aila. 2020. Analyzing and improving the image quality of StyleGAN. In *Proceedings of the IEEE/CVF conference on computer vision and pattern recognition*. 8110–8119.
- [39] Andre Kassis and Urs Hengartner. 2023. Breaking Security-Critical Voice Authentication. In *2023 IEEE Symposium on Security and Privacy (SP)*. 951–968. <https://doi.org/10.1109/SP46215.2023.10179374>
- [40] Diederik P Kingma and Max Welling. 2013. Auto-encoding variational bayes. *arXiv preprint arXiv:1312.6114* (2013).
- [41] Vejay Lalla, Adine Mitran, and Zach Harned. 2022. Artificial intelligence: deepfakes in the entertainment industry. https://www.wipo.int/wipo_magazine/en/2022/02/article_0003.html.
- [42] L. Li, J. Bao, T. Zhang, H. Yang, D. Chen, F. Wen, and B. Guo. 2020. Face X-Ray for More General Face Forgery Detection. In *2020 IEEE/CVF Conference on Computer Vision and Pattern Recognition (CVPR)*. IEEE Computer Society, Los Alamitos, CA, USA, 5000–5009. <https://doi.org/10.1109/CVPR42600.2020.00505>
- [43] Tsung-Yi Lin, Michael Maire, Serge Belongie, James Hays, Pietro Perona, Deva Ramanan, Piotr Dollár, and C Lawrence Zitnick. 2014. Microsoft coco: Common objects in context. In *Computer Vision—ECCV 2014: 13th European Conference, Zurich, Switzerland, September 6–12, 2014, Proceedings, Part V* 13. Springer, 740–755.
- [44] Shaohui Liu, Yi Wei, Jiwen Lu, and Jie Zhou. 2018. An improved evaluation framework for generative adversarial networks. *arXiv preprint arXiv:1803.07474* (2018).
- [45] Nils Lukas, Abdulrahman Diaa, Lucas Fenaux, and Florian Kerschbaum. 2024. Leveraging Optimization for Adaptive Attacks on Image Watermarks. In *The Twelfth International Conference on Learning Representations*.
- [46] Nils Lukas and Florian Kerschbaum. 2023. PTW: Pivotal Tuning Watermarking for Pre-Trained Image Generators. In *32nd USENIX Security Symposium (USENIX Security 23)*. USENIX Association, Anaheim, CA, 2241–2258. <https://www.usenix.org/conference/usenixsecurity23/presentation/lukas>
- [47] Francesco Marra, Diego Gragnaniello, Luisa Verdoliva, and Giovanni Poggi. 2019. Do GANs leave artificial fingerprints?. In *2019 IEEE conference on multimedia information processing and retrieval (MIPR)*. IEEE, 506–511.
- [48] Falko Matern, Christian Riess, and Marc Stamminger. 2019. Exploiting visual artifacts to expose deepfakes and face manipulations. In *2019 IEEE Winter Applications of Computer Vision Workshops (WACVW)*. IEEE, 83–92.
- [49] S. Pereira and T. Pun. 2000. Robust template matching for affine resistant image watermarks. *IEEE Transactions on Image Processing* 9, 6 (2000), 1123–1129. <https://doi.org/10.1109/83.846253>

[50] Fabi Prezja, Juha Paloneva, Ilkka Pölönen, Esko Niinimäki, and Sami Äyrämö. 2022. DeepFake knee osteoarthritis X-rays from generative adversarial neural networks deceive medical experts and offer augmentation potential to automatic classification. *Scientific Reports* 12, 1 (2022), 18573.

[51] Yuyang Qian, Guojun Yin, Lu Sheng, Zixuan Chen, and Jing Shao. 2020. Thinking in frequency: Face forgery detection by mining frequency-aware clues. In *European conference on computer vision*. Springer, 86–103.

[52] Robin Rombach, Andreas Blattmann, Dominik Lorenz, Patrick Esser, and Björn Ommer. 2022. High-resolution image synthesis with latent diffusion models. In *Proceedings of the IEEE/CVF conference on computer vision and pattern recognition*. 10684–10695.

[53] Mehrdad Saberi, Vinu Sankar Sadasivan, Keivan Rezaei, Aounon Kumar, Atoosa Chegini, Wenxiao Wang, and Soheil Feizi. 2024. Robustness of AI-Image Detectors: Fundamental Limits and Practical Attacks. In *The Twelfth International Conference on Learning Representations*.

[54] Chitwan Saharia, William Chan, Saurabh Saxena, Lala Li, Jay Whang, Emily L. Denton, Kamyar Ghasemipour, Raphael Gontijo Lopes, Burcu Karagol Ayan, Tim Salimans, et al. 2022. Photorealistic text-to-image diffusion models with deep language understanding. *Advances in Neural Information Processing Systems* 35 (2022), 36479–36494.

[55] Axel Sauer, Katja Schwarz, and Andreas Geiger. 2022. StyleGAN-XL: Scaling StyleGAN to Large Diverse Datasets. *arXiv.org abs/2201.00273*. <https://arxiv.org/abs/2201.00273>

[56] ShieldMnt. 2021. Invisible Watermark: Python library for invisible image watermark. <https://github.com/ShieldMnt/invisible-watermark>.

[57] Jessica Silbey and Woodrow Hartzog. 2018. The upside of deep fakes. *Md. L. Rev.* 78 (2018), 960.

[58] Jascha Sohl-Dickstein, Eric Weiss, Niru Maheswaranathan, and Surya Ganguli. 2015. Deep unsupervised learning using nonequilibrium thermodynamics. In *International conference on machine learning*. PMLR, 2256–2265.

[59] Vera Sorin, Yiftach Barash, Eli Konen, and Eyal Klang. 2020. Creating artificial images for radiology applications using generative adversarial networks (GANs)–a systematic review. *Academic radiology* 27, 8 (2020), 1175–1185.

[60] Matthew Tancik, Ben Mildenhall, and Ren Ng. 2020. StegaStamp: Invisible Hyperlinks in Physical Photographs. In *IEEE Conference on Computer Vision and Pattern Recognition (CVPR)*.

[61] Florian Tramèr, Alexey Kurakin, Nicolas Papernot, Ian Goodfellow, Dan Boneh, and Patrick McDaniel. 2017. Ensemble adversarial training: Attacks and defenses. *arXiv preprint arXiv:1705.07204* (2017).

[62] Chunpeng Wang, Qixian Hao, Shuijiang Xu, Bin Ma, Zhiqiu Xia, Qi Li, Jian Li, and Yun-Qing Shi. 2022. RD-IWAN: Residual Dense Based Imperceptible Watermark Attack Network. *IEEE Transactions on Circuits and Systems for Video Technology* 32, 11 (2022), 7460–7472. <https://doi.org/10.1109/TCSVT.2022.3188524>

[63] Yuxin Wen, John Kirchenbauer, Jonas Geiping, and Tom Goldstein. 2023. Tree-Rings Watermarks: Invisible Fingerprints for Diffusion Images. In *Thirty-seventh Conference on Neural Information Processing Systems*.

[64] Xi Wu, Zhen Xie, YuTao Gao, and Yu Xiao. 2020. Sstnet: Detecting manipulated faces through spatial, steganalysis and temporal features. In *ICASSP 2020-2020 IEEE international conference on acoustics, speech and signal processing (ICASSP)*. IEEE, 2952–2956.

[65] Ning Yu, Vladislav Skripniuk, Sahar Abdelnabi, and Mario Fritz. 2021. Artificial Fingerprinting for Generative Models: Rooting Deepfake Attribution in Training Data. In *IEEE International Conference on Computer Vision (ICCV)*.

[66] Ning Yu, Vladislav Skripniuk, Dingfan Chen, Larry S. Davis, and Mario Fritz. 2022. Responsible Disclosure of Generative Models Using Scalable Fingerprinting. In *International Conference on Learning Representations*. <https://openreview.net/forum?id=sOK-zS6WHB>

[67] Chaoning Zhang, Philipp Benz, Adil Karjauv, Geng Sun, and In So Kweon. 2020. Udh: Universal deep hiding for steganography, watermarking, and light field messaging. *Advances in Neural Information Processing Systems* 33 (2020), 10223–10234.

[68] Kevin Alex Zhang, Lei Xu, Alfredo Cuesta-Infante, and Kalyan Veeramachaneni. 2019. Robust Invisible Video Watermarking with Attention. (2019). [arXiv:1909.01285 \[cs.MM\]](https://arxiv.org/abs/1909.01285)

[69] Richard Zhang, Phillip Isola, Alexei A Efros, Eli Shechtman, and Oliver Wang. 2018. The Unreasonable Effectiveness of Deep Features as a Perceptual Metric. In *CVPR*.

[70] Hanqing Zhao, Wenbo Zhou, Dongdong Chen, Tianyi Wei, Weiming Zhang, and Nenghai Yu. 2021. Multi-attentional deepfake detection. In *Proceedings of the IEEE/CVF conference on computer vision and pattern recognition*. 2185–2194.

[71] Xuandong Zhao, Kexun Zhang, Zihao Su, Saastha Vasani, Ilya Grishchenko, Christopher Kruegel, Giovanni Vigna, Yu-Xiang Wang, and Lei Li. 2023. Invisible Image Watermarks Are Provably Removable Using Generative AI. In *ICML 2023 Workshop on Challenges in Deploying Generative AI*.

[72] Yunqing Zhao, Tianyu Pang, Chao Du, Xiao Yang, Ngai-Man Cheung, and Min Lin. 2023. A recipe for watermarking diffusion models. *arXiv preprint arXiv:2303.10137* (2023).

[73] Yunqing Zhao, Tianyu Pang, Chao Du, Xiao Yang, Ngai-Man Cheung, and Min Lin. 2023. A recipe for watermarking diffusion models. *arXiv preprint arXiv:2303.10137* (2023).

[74] Jiren Zhu, Russell Kaplan, Justin Johnson, and Li Fei-Fei. 2018. HiDDeN: Hiding Data with Deep Networks. In *Proceedings of the European Conference on Computer Vision (ECCV)*.

A APPENDIX

A.1 Generative AI

Leading image generators fall under three classes:

Generative Adversarial Networks (GANs). A GAN [24] consists of a generator $\mathcal{G} : \mathcal{Z} \rightarrow \mathcal{X}$, where \mathcal{Z} is a space of latent codes from which \mathcal{G} generates images in \mathcal{X} that represents this desired image distribution, and a discriminator $\mathcal{D} : \mathcal{X} \rightarrow (0, 1]$, that tells apart real from fake images. In practice, \mathcal{D} outputs a probability for the sample being real or fake. The two are simultaneously trained s.t \mathcal{D} learns to accurately discern between real images and those outputted by \mathcal{G} , while \mathcal{G} is proactively improved to fool the continuously-enhanced discriminator \mathcal{D} by generating more real-looking data, pushing it to synthesize high-quality images. Afterward, \mathcal{G} can be used to generate images from random latent codes. NVIDIA’s StyleGAN [37, 38, 55] is a family of advanced GANs.

Diffusion Models (DMs). DMs [58] consist of two stages: a forward (diffusion) pass and a backward (reverse) pass. During the forward pass, each image x_0 is iteratively noised for a number of steps T . The output x_t of the t^{th} step is $x_t = \sqrt{1 - \beta_t}x_{t-1} + \sqrt{\beta_t}z_t$ where $\{z_t\}$ are IID-sampled variances, and $\{\beta_t\} \in (0, 1)$ are fixed constants. When $T \rightarrow \infty$, the output x_T converges to a pure Gaussian. Yet, as T is practically finite, x_T retains information regarding the initial x_0 , enabling the use of DMs that strive to learn the inverse procedure to reconstruct this x_0 from this x_T . By learning to undo the diffusion, DMs gain the ability to focus on fine-grained details, allowing them to later synthesize images of unparalleled quality. Synthesis starts from a random Gaussian and applies the backward procedure for several steps. An example is *OpenAI’s DALL·E* [2].

Latent Diffusion Models (LDMs). LDMs [52] are DMs that do not operate in the pixel space but rather deploy an encoder \mathcal{E} and a decoder \mathcal{D} . \mathcal{E} transforms images into compressed latent representations on which the above diffusion passes are performed. \mathcal{D} then transforms the reconstructed latents back into images. LDMs offer several advantages over DMs such as efficiency and enhanced resolution. A popular LDM is *Stability AI’s Stable Diffusion* [3].

Conditional Generation. All generators can be used in a conditional manner, designed to accept additional information that influences their output, such as text describing the desired content [2, 3] or the identity of the person whose picture is to be synthesized [11].

A.2 Details Regarding The Watermarking Schemes’ Configurations

The watermark lengths used for each of the schemes we study are in Table 4. Recall that we use the official implementations provided by the authors of each scheme, who found these to be optimal. The systems were, therefore, pretrained to operate using these lengths.

A.3 UnMarker’s Hyperparameters

Below we present *UnMarker*’s hyperparameter considerations.

Table 4: Watermark lengths. *TRW*’s watermarks are not binary sequences, and thus, this metric is not applicable

Scheme	Watermark Length (# bits)
<i>Yu1</i>	128
<i>Yu2</i>	100
<i>HiDDeN</i>	30
<i>PTW</i>	40
<i>StableSignature</i>	48
<i>StegaStamp</i>	100
<i>TRW</i>	NA

High-frequency Disruptions (Stage 1— §5.1): We use the *Alex-Net*-based *LPIPS* [69] for small images (128×128) and the *DVL* [17] perceptual loss (ℓ_p) for larger sizes. As we maximize ℓ_{F0} , we want to set the threshold t_p to the largest value at which the changes still retain similarity and do not lead to artifacts. This t_p depends on ℓ_p and the image size (resolution). For small images optimized using the *Alex-Net*-based loss, this optimal point is $t_p = 5 \cdot 10^{-4}$. Since larger images require a different loss (*DVL*), similar thresholds do not indicate the same degree of resemblance. For 256×256 images, we find $t_p = 4 \cdot 10^{-2}$ best achieves the above goals, while for larger images we have $t_p = 10^{-4}$. Next, we select the initial c_p that balances the spectral and visual losses. We want this starting value to be significant to assign a large weight to ℓ_p and ensure visual similarity is not violated, after which it can be decreased to allow the spectral loss to be more dominant while still ensuring this property. This initial setting only affects the time until it converges and must be empirically determined to speed up the process. We found an initial $c_p = 10^6$ optimal for small images that use the *Alex-Net*-based *LPIPS*. For *DVL*, this was set at 10^6 when the size is above 256×256 as these images require the *DVL* loss to be extremely small (10^{-4}), while for 256×256 images, it can be far smaller (10^{-2}).

The $\|\cdot\|_2$ component prevents unwanted peaks (see §5.1). Its threshold depends on the size and chosen *LPIPS*. While the *LPIPS* thresholds guarantee visual similarity to the extent that the images will look similar up to, potentially, such peaks, $\|\cdot\|_2$ ’s thresholds must eliminate these singular points when the *LPIPS* thresholds are met. We empirically selected these $\|\cdot\|_2$ thresholds: for 128×128, we have $t_{\|\cdot\|_2} = 10^{-4}$, while 256×256 images allow $t_{\|\cdot\|_2} = 3 \cdot 10^{-5}$, and larger images operate at $t_{\|\cdot\|_2} = 10^{-4}$. We report the normalized thresholds (divided by the image size). In practice, they increase with the size since larger images accommodate stronger perturbations without visible cues. $c_{\ell_{\|\cdot\|_2}}$ multiplies this $\|\cdot\|_2$ when its threshold is violated to strongly steer the procedure away from these boundaries. This is not determined through a binary search, as we want it to constantly have the same effect. It should be selected to accomplish this without undoing the majority of the previous iterations’ effects. By tracking the losses, we arrive at $c_{\ell_{\|\cdot\|_2}} = 0.6$.

By monitoring the spectral loss, we can determine when it stops increasing for each value of c_p and, similarly, the number of steps after which updating c_p does not result in further improvements. This yields 5000 iterations for images smaller or larger than 256×256, while for this size, the loss plateaus after 2000 iterations. The number of binary search steps is 2 for sizes $\leq 256 \times 256$ and 4 otherwise.

We use the *Adam* optimizer with learning rate $2 \cdot 10^{-4}$, reduced by 0.5 when no improvement (above 10^{-4}) to the spectral loss occurs

for 10 iterations. We clip the gradients at $5 \cdot 10^{-3}$ for *DVL* and $5 \cdot 10^{-2}$ for the *Alex-Net*-based loss to ensure they do not dominate the process and allow the spectral loss to influence the results.

Low-frequency Disruptions (Stage 2— §5.2): Each filter $OF_{\mathcal{K}_t^*, x_w, \sigma_{ct}}^t$ is characterised by two hyperparameters: dimensionality $M_t \times N_t$ of the kernel \mathcal{K}_t^* and permissiveness σ_{ct} . We find $\sigma_{ct} = 5 \cdot 10^{-2}$ always optimal. When choosing the kernel sizes and number of filters T , resources can become a bottleneck as we have a kernel per pixel, making each filter scale as the number of pixels multiplied by the kernel size. We found $T = 9$ with different kernel sizes defeats all studied systems. This architecture was chosen (semi-randomly) to target various potential geometries of the watermark under our computational limitations (40 GB A100 GPU) but can be further optimized (additional layers) with better hardware. However, our findings indicate that this may not be necessary. The chosen sizes (in sequential order) are (21, 5), (5, 5), (17, 33), (7, 7), (47, 5), (33, 17), (17, 17), (5, 5) and (3, 3).

The spectral loss (see eq. (6)) consists of *MPL* and *FRL*. While we maximize both, *FRL* is effectively a regularization term supporting *MPL*— see §5.2.4. Hence, we focus on *MPL*, deeming a sample to be optimal if it maximizes this loss. Yet, λ_{FRL} must account for *FRL*, ensuring the outputs meet the conditions it enforces. $\lambda_{FRL} = 5$ was found optimal, but it can be adjusted if the two components do not meet expectations (see §5.2.4). We found the $\|\cdot\|_2$ term’s coefficient $\lambda_{\|\cdot\|_2} = 2.5 \cdot 10^{-4}$ ideal but it can be calibrated similarly.

For low-frequencies, *DVL* is universally applicable (see §5.1). The remaining unknowns were chosen based on similar considerations to those for our high-frequency stage. As low-frequency perturbations do not risk introducing unwanted peaks, these parameters can be selected uniformly with little regard to the image size. The exception is the perceptual threshold t_{DVL} , as smaller images (256×256 and below) are more sensitive to structural changes (as opposed to high-frequency perturbations that can be masked by these images’ low resolution), exhibiting (minor) visible differences for $t_{DVL} > 10^{-3}$, while larger images can withstand three times this change. With an initial $c_{DVL} = 10^6$, a single step running for 500 iterations is sufficient. We use *Adam* with a 10^{-2} learning rate for the filters and $2 \cdot 10^{-3}$ for the modifier δ , decayed by 0.99 if *MPL* fails improve by $5 \cdot 10^{-2}$ for 10 iterations. As *DVL*’s impact is weakened due to the structural changes this process induces, we allow its gradients to be more dominant, clipped at 1.0.

Filters operate on all image channels identically. As the reason behind including a direct modifier δ here is the filters’ ability to smoothen these otherwise high-frequency changes, it must affect all channels similarly for them to achieve this outcome. Thus, we use a (*gray-scale*) modifier δ that applies the same changes to all channels. Finally, watermarks exist in the spectral amplitudes rather than phases. While manipulating amplitudes impacts the texture and, therefore, results in less critical changes, phase modifications are more visible (see §4.1.1). Hence, we should ideally restrict our filters to manipulate these magnitudes. The frequency response of a filter does not change the phase if and only if it is even-symmetric (identical to the reflections of each of its quadrants across both axes). While this holds for *basic* (convolutional) filters, ours will converge to similar kernels for neighboring pixels that are of equal visual importance and can be altered similarly, indicating that each region

Table 5: Performance of the schemes against basic manipulations. The first row shows the results in the absence of any manipulations. Numbers in parentheses are the detection thresholds, while *Detect* is the portion of images meeting them. For attacks with multiple configurations, lower rows correspond to stronger distortions. * denotes overly-destructive configurations.

Manipulation \ Scheme	Yu1 (61%)		Yu2 (63%)		HiDDeN (73%)		PTW (70%)		StableSignature (69%)		StegaStamp (63%)		TRW (0.0141)	
	Bit Acc↑	Detect↑	Bit Acc↑	Detect↑	Bit Acc↑	Detect↑	Bit Acc↑	Detect↑	Bit Acc↑	Detect↑	Bit Acc↑	Detect↑	Inv. Dist.↑	Detect↑
None	98.42%	100%	99.71%	100%	99.16%	100%	97.96%	100%	98.97%	100%	99.95%	100%	0.022	100%
Cropping	74.56%	100%	53.71%	0%	86.84%	100%	93.9%	100%	97.86%	100%	93.96%	100%	0.0155	100%
<i>std. = 0.5</i>	98.13%	100%	99.55%	100%	96.45%	100%	96.93%	100%	98.52%	100%	99.95%	100%	0.0221	100%
<i>std. = 1.0</i>	94.6%	100%	99.73%	100%	62.15%	5.00%	82.25%	100%	86.65%	99%	99.88%	100%	0.0207	100%
Blur	87.91%	100%	99.32%	100%	75.6%	76%	94.41%	100%	96.38%	100%	99.91%	100%	0.0212	100%
<i>color std. = 0.1</i>	85.32%	100%	99.43%	100%	56.12%	0%	78.66%	98%	71.25%	69%	99.93%	100%	0.02	100%
<i>color std. = 1.0*</i>	84.9%	100%	99.62%	100%	53.81%	0%	76.42%	92%	66.54%	50%	99.93%	100%	0.0199	100%
<i>color std. = 5.0*</i>	85.86%	100%	99.16%	100%	89.34%	98%	74.92%	93%	98.83%	100%	99.83%	100%	0.0207	100%
Quantization	82.51%	100%	98.7%	100%	86.51%	98%	68.34%	46%	99.04%	100%	99.8%	100%	0.0201	100%
<i>factor = 8</i>	89.58%	100%	99.55%	100%	70.73%	43%	87.66%	100%	97.68%	99%	99.94%	100%	0.0215	100%
<i>factor = 10</i>	76.38%	100%	93.15%	100%	66.48%	16%	72.17%	76%	90.66%	100%	99.89%	100%	0.202	100%
JPEG														

will behave as if it were “convolved with a basic kernel”. Thus, our filters should possess this even-symmetry property. Accordingly, instead of optimizing all kernel weights, we focus only on the first quadrant of each filter and then reflect it across both axes.

A.4 Baseline Results Against Naive Image Manipulations

Most systems are robust to all *practical* manipulations. Interestingly, *Yu2* breaks completely under *cropping*. This result does not contradict the original paper [65]; The authors watermark several generators yet only evaluate a single *ProGAN* [35] architecture under manipulations, whereas we chose their advanced *StyleGAN2* [38] model. Overall, our observations reveal that, unlike all other schemes, *Yu2* is highly dependent on spatial attributes, making it volatile to manipulations such as *cropping*. However, it remains robust to all other modifications. Several other schemes (*Yu1*, *HiDDeN* and *TRW*) exhibit a considerable drop in the average *bit accuracies* (*inverse distance*) after *cropping*, despite their overall detection rates not being affected. This is not surprising, as the spectral modifications for watermark injection must be spread throughout the image (see §4.1) to minimize visual cues, implying that a portion may be allocated to the background. Yet, they remain robust by restricting most of these changes to central regions.

Yu1, *StegaStamp* and *TRW* resist all manipulations, while *StableSignature* can withstand realistic, non-obtrusive modifications, making it also robust for practical purposes. *PTW* is slightly less powerful since it loses some of its efficacy under even non-destructive operations, such as *Quantization* with a factor of 10 and *JPEG* with quality 80 that decrease its performance to 46% and 76%, respectively. *HiDDeN* exhibits similar behavior, showing resistance to all realistic manipulations, aside from *JPEG* that brings its detection to 43% even when used with a reasonably good quality of 110 or *Blurring* with *std.* = 1.0 that lowers its detection score to 5.0%.

It is not unnatural to see that some *non-semantic* systems (e.g., *PTW*, *HiDDeN* and *StableSignature*) begin to break under spectral manipulations such as *JPEG* that has been shown effective against *heuristics-based* watermarks (see §2) operating in the spectrum as well, *Blurring* or *Quantization*. As explained in §4.1, constructing spectral *non-semantic* watermarks should be done in an input-specific manner that is also persistent, which is a challenging task

that will be restricted to volatile watermarks unless the scheme is sufficiently advanced. This explains why the more sophisticated *StableSignature* and *PTW* outperform *HiDDeN* in this department. Yet, allowing for more severe spectral manipulations by applying stronger (*Guided*) *Blurring* breaks *StableSignature* as well, although this experiment is only included to demonstrate this phenomenon that attests to the spectral nature of these watermarks and does not make for a valid attack, as explained in §6.1. Similarly, *Quantization* can cause sharp pixel shifts and affect the signal’s smoothness, introducing high-frequency noise, explaining *PTW*’s vulnerability.

For all naive manipulations, our findings are comparable to those attained by the authors of the schemes that evaluate the same attacks with similar parameters. The only exceptions are *Gaussian Blurring* with *std.*=1.0 against *HiDDeN* and *JPEG* with *quality*=80 against *PTW*, for which we observed a non-negligible drop in the *bit accuracies* compared to these original works. We hypothesize that this is due to us using a different kernel size for the *Gaussian* filter (the authors of *HiDDeN* do not report this parameter) and a different implementation of the *JPEG* algorithm compared to *PTW*.

A.5 Effects of Adversarial Filtering

Table 6: *UnMarker*’s performance against *semantic* schemes with and without using optimizable filters.

Attack \ Scheme	StegaStamp (63%)				TRW (0.0141)			
	FID↓	LPIPS↓	Bit Acc↓	Detect↓	FID↓	LPIPS↓	Inv. Dist.↓	Detect↓
UnMarker with filters	34.69	0.08	61.49%	43%	60.73	0.1	0.014	40%
without filters	30.45	0.04	93.13%	100%	49.59	0.04	0.0147	86%

Despite our thorough analysis substantiating the choice to perform filtering-based optimizations to defeat low-frequency watermarks, this attack has two major changes compared to our high-frequency disruptive procedure. While one introduces the filtering-based approach, the other replaces the loss function that is obviously unsuitable for low-frequency distortions, as explained in §5.2.

The reader may wonder whether replacing the loss function alone can achieve the same outcome, eliminating the need for computationally expensive filters. Yet, based on our arguments explaining how direct input optimizations can only be of limited applicability against low-frequency watermarks due to their non-systemic

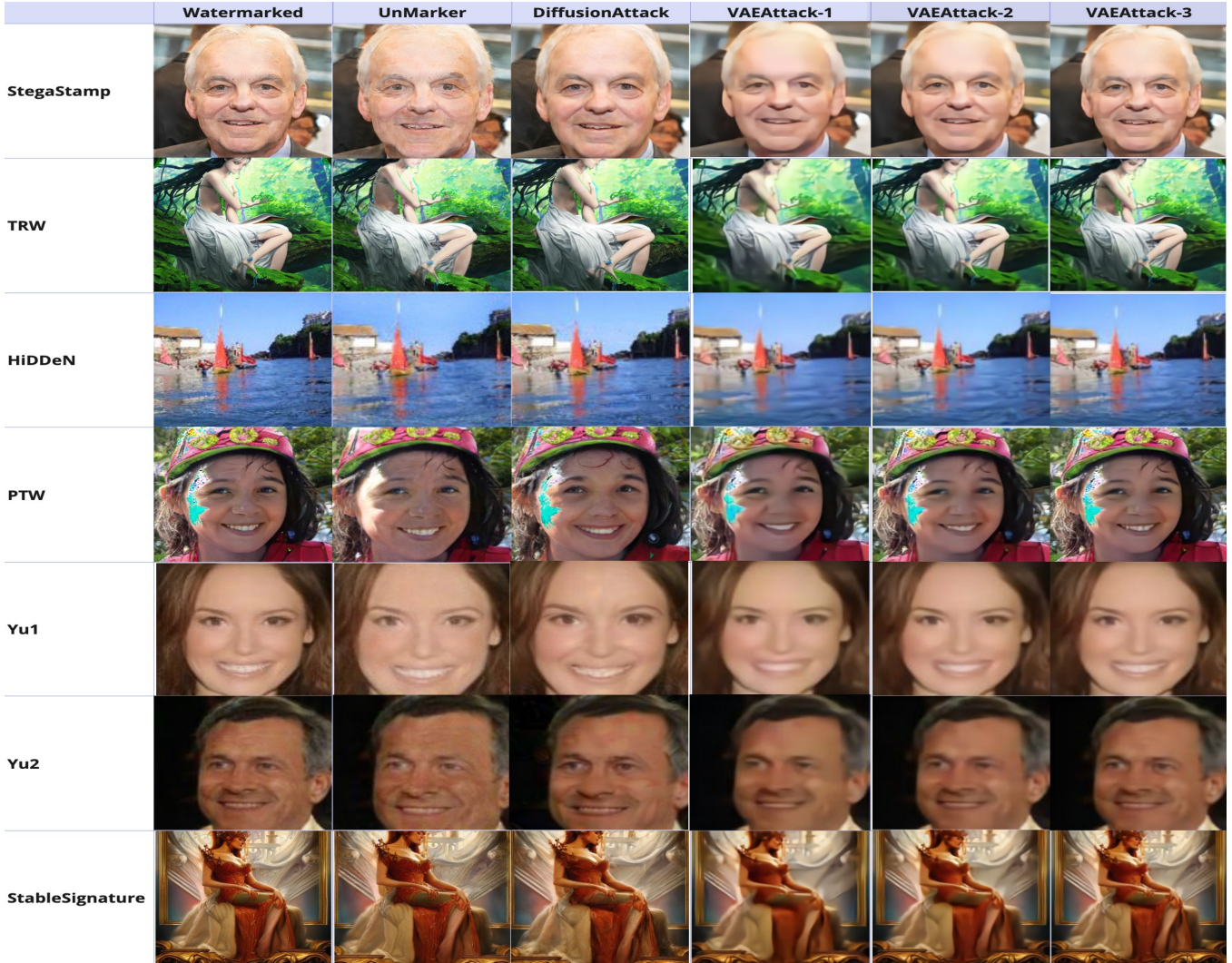


Figure 4: Outputs of the three removal attacks. The *VAEAttack* over-smooths images, resulting in them losing crucial information and occasionally looking cartoonish. Compared to the *DiffusionAttack*, *UnMarker*’s outputs better resemble the watermarked images. The *DiffusionAttack* also introduces semantic incoherences such as additional teeth in the case of *PTW* and omits identifying details such as freckles on the forehead for *StegaStamp*. *PTW*’s watermarked image itself is of inferior quality with an unnatural patch. The *DiffusionAttack* retains this artifact while *UnMarker* eliminates it, enhancing the image.

nature, this is not the case. To validate this claim, we compare *UnMarker* against the two *semantic* (low-frequency) schemes, *TRW* and *StegaStamp*, with and without our filters. In both experiments, the loss is the same low-frequency function from §5.2.4.

The results in Table 6 unequivocally prove the filters necessary. While *TRW*, which the previous experiments prove more fragile, experiences a slight drop in performance without the filters, including them is far more effective, bringing its detection rate to 40% (compared to 86% without filters). *StegaStamp* remains completely unaffected when the filters are excluded, retaining a 100% detection rate. With our filters, this drops to 43%. We also verified that the inability of the filter-free attack to break these schemes persists even if the perturbation budget slightly increases. Note that without

filters, we obtain slightly better similarity scores since the filters encourage necessary structural changes. Yet, even with the filters, these scores still prove that *UnMarker* retains quality.

A.6 Outputs of *UnMarker* vs. The SOTA

Fig. 4 displays examples of watermarked images and the outputs obtained by subjecting them to advanced removal attacks.